UNIVERSITÀ DEGLI STUDI DI NAPOLI
"FEDERICO II"

Scuola Politecnica e delle Scienze di Base

Area Didattica di Scienze Matematiche Fisiche e Naturali

Dipartimento di Fisica "Ettore Pancini"

Laurea Magistrale in Fisica

Sensitivity study of $B \to \tau\nu$ decay with Hadronic Tagging at the Belle II Experiment

Relatori:
Prof. Gugliemo De Nardo
Dr. Mario Merola

Candidato:
Giovanni Gaudino
Matr. *N*94000616

Anno Accademico 2020/2021

A mamma e papà.

INTRODUCTION

The Standard Model of particle physics is a theory describing the properties of all known elementary particles and the interaction among them. This theory has been modelled over the years and nowadays it is able to explain almost all experimental results. With the discovery of the Higgs boson at the Large Hadron Collider (LHC) in 2012, another missing piece in the Standard Model was discovered. Although this theory was proven successful over time, there are still phenomena which cannot be described by the Standard Model, these kind of phenomena are part of the physics beyond the Standard Model. In chapter 1 a brief description of Flavour Physics and how the Standard Model explains the quarks mixing are given.
An important experiment pursuing the precise measurement of the Standard Model parameters as well as the search for physics beyond the Standard Model is the Belle II experiment. At the SuperKEKB collider, where the Belle II detector is installed, electrons and positrons interact at a center of mass energy equal to the $\Upsilon(4S)$ mass. This resonance decays roughly 96% into a B meson pair without any additional particle. The decay products of the B mesons are then measured by the Belle II detector. In chapter 2, a detailed description of the SuperKEKB collider and the Belle II experiment is provided.
B mesons can decay via various decay channels. Leptonic B decays, like the $B \to \tau\nu_\tau$ decay, which investigation is presented in this thesis, are really interesting since they could be probes to physics beyond the Standard Model, because precise theoretic estimate ara available. For example, the observation of the $B \to \tau\nu_\tau$ decay could lead to first hints for charged Higgs bosons or other new mediators. But in contrast, leptonic B meson decays are difficult to observe experimentally since they are highly suppressed due to Cabibbo-Kobayashi-Maskawa (CKM) matrix, which explains how quarks mix each other. In chapter 3 a detailed explanation about the theory behind B mesons and how leptonic decays could be a very important window for new physics is given.
In the chapter 4, the sensitivity of the Belle II experiment to the search for $B \to \tau\nu_\tau$ decays is described. The $B \to \tau\nu_\tau$ signal is searched using a Monte Carlo sample with an equivalent integrated luminosity of $1\,\mathrm{ab}^{-1}$ of data and using the 1-prong decays of the τ lepton[1]:

- $\tau \to e\nu\nu$
- $\tau \to \mu\nu\nu$

1 From this moment on, the neutrino subscripts will not be reported, since only leptonic number conservation phenomena will be considered.

- $\tau \to \pi\nu$
- $\tau \to \rho\nu$

The signal events extraction has been obtained through a signal selection optimization, in which many discriminating variables have been analyzed and the best selection requirements have been found. Finally a study on the Branching Ratio measurement has been performed on many pseudo-experiments in a range of integrated luminosity from $100\,\mathrm{fb}^{-1}$ to $1000\,\mathrm{fb}^{-1}$ with an extended maximum likelihood fit for each of the four τ decay modes.

CONTENTS

1 THEORETICAL CONCEPTS AND PHYSICS AT BELLE II 1
1.1 Flavour physics in a nutshell 1
1.1.1 Experimental evidences 1
1.1.2 GWS Model of Weak Interaction 2
1.1.3 Fermions coupling with gauge bosons 3
1.1.4 Fermions Coupling with Higgs bosons 6
1.1.5 Standard Parametrization of the CKM Matrix 10
1.1.6 The Unitarity Triangle 11
2 BELLE II EXPERIMENT 13
2.1 The SuperKEKB accelerator 14
2.1.1 Beam-Induced Background 16
2.2 Overview of the Belle II detector 16
2.3 Tracking detectors 18
2.3.1 Silicon-pixel vertexing detector 18
2.3.2 Silicon-microstrip vertexing detector 19
2.3.3 Central drift chamber 19
2.3.4 Particle-identification detectors 20
2.3.5 Time of propagation counter 20
2.3.6 Aerogel ring-imaging Cherenkov 21
2.3.7 Electromagnetic calorimeter 22
2.3.8 K_L^0 and muon detection system 22
2.3.9 Trigger System 22
3 B MESON PHYSICS 24
3.1 Production 24
3.2 Oscillations 25
3.2.1 $\mathcal{CP}$ violation in the B-meson system 26
3.3 B Meson Physics: Leptonic Decays 27
3.4 τ Decays 29
4 SEARCH FOR $B \to \tau\nu$ DECAY 30
4.1 Computing Environment 30
4.2 Dataset and MC Samples 31
4.2.1 Full Event Interpretation 31
4.3 Signal Events Selection 34
4.3.1 Signal Selection Optimization 41
4.4 $B \to \tau\nu$ Branching Ratio Measurement 43
4.4.1 Fit Process 43
4.4.2 Measurement Optimization 45
4.4.3 Efficiency Measurement 49

4.5 Belle II sensitivity on $B \to \tau\nu$ Branching Ratio 52
CONCLUSIONS 58
BIBLIOGRAPHY 59

1 THEORETICAL CONCEPTS AND PHYSICS AT BELLE II

1.1 FLAVOUR PHYSICS IN A NUTSHELL

1.1.1 Experimental evidences

The term *Flavour* was first used in particle physics in the context of the quark model of hadrons. It was coined in 1971 by Murray Gell-Mann and his student at the time, Harald Fritzsch, at a Baskin-Robbins ice-cream store in Pasadena. Just as ice cream has both color and flavor so do quarks[5]. "Flavour" is now used slightly more generally to denote the species of any Standard Model (SM) fermion, both quarks and leptons and the "Flavour" physics studies how quarks and leptons mix each other.
A cornerston of this physics field is the article written in 1970, in which Sheldon Lee Glashow, Ioannis Iliopoulos and Luciano Maiani proposed a physics model about weak interactions, including four quark in a $SU(2)$ group.
Till then, only three quarks were discovered (u, d and s), related to each other by Nicola Cabibbo mechanism, which in 1963 theorized the universality of the V-A structure including a quark mixing between the negative charged quarks (d and s), initiating the Flavour Physics [6].
In GIM mechanism, quarks were gathered together in two doublets of $SU(2)$.

$$\begin{pmatrix} u \\ d' \end{pmatrix} \qquad \begin{pmatrix} c \\ s' \end{pmatrix} \tag{1.1}$$

where

$$\begin{pmatrix} d' \\ s' \end{pmatrix} = \begin{bmatrix} \cos\vartheta_C & \sin\vartheta_C \\ -\sin\vartheta_C & \cos\vartheta_C \end{bmatrix} \begin{pmatrix} d \\ s \end{pmatrix} \tag{1.2}$$

The new parameter ϑ_C (Cabibbo angle) in (1.2) was measured in 1963, studying former the ratio about the width of $\pi \to \mu\nu$ and $K \to \mu\nu$ that is proportional to $\tan^2\vartheta_C$, latter the decay $K \to \pi^0 e\nu$, obtaining the same result of $\vartheta = 0.26 = 13°$.
In the following years, the improvement of the particle accelerator was so important that other two quarks were discovered:

- b quark, discovered in 1977, by Lederman [10].
- t quark, discovered in 1995, by CMS and DØ collabation [1].

1.1.2 GWS Model of Weak Interaction

Experimental evidences, briefly explained in 1.1, are now direct consequences of a model, called Standard Model, which tries to explain three out of four fundamental interactions by using the mathematical formalism of group theory and the quantum field theory.
In this thesis, we will explain only the electroweak interaction of the Standard Model. This kind of interaction is explained through the symmetries of the group $SU(2)_L \otimes U(1)$, where L stays for *left*, since a pure weak interaction is possible only between left helicity particles (spin and momentum in opposite direction).
In GWS Model, fundamental fermions are represented by weak isospin doublets.

$$\begin{matrix} t, t_3 = 1/2, +1/2 \\ t, t_3 = 1/2, -1/2 \end{matrix} \quad \begin{pmatrix} \nu_e \\ e^- \end{pmatrix}_L \quad \begin{pmatrix} \nu_\mu \\ \mu^- \end{pmatrix}_L \quad \begin{pmatrix} \nu_\tau \\ \tau^- \end{pmatrix}_L \tag{1.3}$$

$$\begin{matrix} t, t_3 = 1/2, +1/2 \\ t, t_3 = 1/2, -1/2 \end{matrix} \quad \begin{pmatrix} u \\ d' \end{pmatrix}_L \quad \begin{pmatrix} c \\ s' \end{pmatrix}_L \quad \begin{pmatrix} t \\ b' \end{pmatrix}_L \tag{1.4}$$

L subscript stays for the eigenvector of the helicity (assuming that fermions are massless, because a massive fermion would break the simmetry of the group). This can be summarized in this equation

$$f_L = \frac{1}{2}(1 - \gamma_5) f \quad \text{where} \quad \gamma_5 = \gamma_0\gamma_1\gamma_2\gamma_3$$

Taking in account quark mixing, eigenstates of $SU(2)$ are different from mass eigenstates and they are connected by the Cabibbo-Kobayashi-Maskawa matrix (an extension of the Cabibbo rotation)

$$\begin{pmatrix} d' \\ s' \\ b' \end{pmatrix} = V_{CKM} \begin{pmatrix} d \\ s \\ b \end{pmatrix}$$

Right particles are in $SU(2)$ singlets, characterized by a quantum number $t = 0$.

$$t = 0 \qquad e^-_R, \mu^-_R, \tau^-_R, u_R, d'_R, c_R, s'_R, t_R, b'_R, \nu_R^{(e,\mu,\tau)}$$

Antiparticles follow the same logic, in weak interaction only right component of anti-fermions acts.

$$\begin{matrix} t, t_3 = 1/2, +1/2 \\ t, t_3 = 1/2, -1/2 \end{matrix} \quad \begin{pmatrix} e^+ \\ \overline{\nu}_e \end{pmatrix}_R \quad \begin{pmatrix} \mu^+ \\ \overline{\nu}_\mu \end{pmatrix}_R \quad \begin{pmatrix} \tau^+ \\ \overline{\nu}_\tau \end{pmatrix}_R \tag{1.5}$$

$$\begin{matrix} t, t_3 = 1/2, +1/2 \\ t, t_3 = 1/2, -1/2 \end{matrix} \quad \begin{pmatrix} \overline{d}' \\ \overline{u} \end{pmatrix}_R \quad \begin{pmatrix} \overline{s}' \\ \overline{c} \end{pmatrix}_R \quad \begin{pmatrix} \overline{b}' \\ \overline{t} \end{pmatrix}_R \tag{1.6}$$

In order to unify weak and electromagnetic interaction, $SU(2)_L \otimes U(1)_Y$ was theorized and Y, the "electromagnetic" quantum number, was called *weak hypercharge*, because in order to distinguish weak and electromagnetic interaction at the lowest order, it is necessary a rotation between a $SU(2)$ boson gauge (W_3) and $U(1)_Y$ boson gauge (B).
The Lagrangian of this theory is the following:

$$\mathcal{L} = \sum_{doublets} i\overline{\psi}_L \gamma^\mu \mathcal{D}^L_\mu \psi_L + i\overline{\psi}_R \gamma^\mu \mathcal{D}^R_\mu \psi_R \tag{1.7}$$

where

$$\mathcal{D}^L_\mu = \partial_\mu + ig\frac{\boldsymbol{\tau}}{2} \cdot \mathbf{W}_\mu + ig'\frac{Y}{2}B_\mu \tag{1.8}$$

$$\mathcal{D}^R_\mu = \partial_\mu + ig'\frac{Y}{2}B_\mu \tag{1.9}$$

These gauge fields follows this transformations

$SU(2)_L$	$U(1)_Y$
$\mathbf{W}_\mu \to \mathbf{W}_\mu + \partial_\mu \boldsymbol{\epsilon}(x) + g\boldsymbol{\epsilon}(x) \times \mathbf{W}_\mu$ $B_\mu \to B_\mu$	$\mathbf{W}_\mu \to \mathbf{W}_\mu$ $B_\mu \to B_\mu + \partial_\mu \delta(x)$

Lagrangian becomes

$$\mathcal{L} = \sum_{doublets} \left(i\overline{\psi}_L \gamma^\mu \mathcal{D}^L_\mu \psi_L + i\overline{\psi}_R \gamma^\mu \mathcal{D}^R_\mu \psi_R \right) - \frac{1}{4}\mathbf{G}_{\mu\nu}\mathbf{G}^{\mu\nu} - \frac{1}{4}C_{\mu\nu}C^{\mu\nu} \tag{1.10}$$

where kinetic energy terms have been added

$$C_{\mu\nu} = \partial_\mu B_\nu - \partial_\nu B_\mu \qquad \mathbf{G}_{\mu\nu} = \partial_\mu \mathbf{W}_\nu - \partial_\nu \mathbf{W}_\mu - g\mathbf{W}_\mu \times \mathbf{W}_\nu$$

Nevertheless, physics experiments show that neutral currents do not involve only left-handed particles, for this reason diagonal part of $\boldsymbol{\tau} \cdot \mathbf{W}$, that is $W^{(3)}$, must be mixed with B gauge boson. The result of this mix will be two mass eigenstates. Trivially, the mix can be written like a rotation, in a way that the only free parameter is an angle, called *Weinberg angle*.

$$\begin{pmatrix} A_\mu(\gamma) \\ Z_\mu(Z^0) \end{pmatrix} = \begin{pmatrix} \cos\vartheta_W & \sin\vartheta_W \\ -\sin\vartheta_W & \cos\vartheta_W \end{pmatrix} \begin{pmatrix} B_\mu \\ W^{(3)}_\mu \end{pmatrix} \tag{1.11}$$

1.1.3 Fermions coupling with gauge bosons

In order to study physics phenomena, the most important component of the Lagrangian in 1.10 is the interactive one.
In this thesis work, leptonic decay of a B meson (composed by a b and u quarks)

are studied. For this purpose, it is necessary a formalism that sum up leptons and quarks interactions. To study pure weak interaction (without some other mix CKM-related) it is easier to only one lepton doublet.

$$\chi_L = \begin{pmatrix} \nu_e \\ e^- \end{pmatrix}_L$$

Defining more clearly only interaction component of the Lagrangian, it is possibile to write

$$\mathcal{L}' = g\overline{\chi}_L \gamma^\mu \frac{\boldsymbol{\tau}}{2} \cdot \boldsymbol{W}_\mu \chi_L - \frac{g'}{2}\overline{\chi}_L \gamma^\mu Y_L B_\mu \chi_L - \frac{g'}{2}\bar{e}_R \gamma^\mu Y_R^{(e)} B_\mu e_R \tag{1.12}$$

that can be simplified using the definition of a current quadrivector

$$\mathcal{L}' = -gJ_\mu^1 W_1^\mu - gJ_\mu^2 W_2^\mu - gJ_\mu^3 W_3^\mu - \frac{g'}{2} j_\mu^Y B^\mu \tag{1.13}$$

where J_μ are isospin weak triplets current and j_μ is weak hypercharge current. Since the electroweak mixing, it is easy to study physics phenomena separating charged currents and neutral currents interactions.

Charged currents

The bosons $W^\pm$ play a role when the interaction Lagrangian change the isospin of the doublets, for this reason charged currents had only τ_1 and τ_2 matrix.

$$gJ_\mu^1 W_1^\mu + gJ_\mu^2 W_2^\mu = g\overline{\chi}_L \gamma_\mu \left[\frac{\tau_1}{2} W_1^\mu + \frac{\tau_2}{2} W_2^\mu\right] \chi_L \tag{1.14}$$

$$= \frac{g}{\sqrt{2}}\overline{\chi}_L \gamma_\mu \left[\tau_+ W^\mu + \tau_- W^{\dagger\mu}\right] \chi_L \tag{1.15}$$

Explaining the charged current Lagrangian, it is possible to obtain the matrix transition element $\mathcal{M}$.

$$-\imath\mathcal{L}'^{CC} = -\imath\frac{g}{\sqrt{2}}\overline{\nu}\gamma^\mu \left(\frac{1-\gamma^5}{2}\right) e W_\mu - \imath\frac{g}{\sqrt{2}}\bar{e}\gamma^\mu \left(\frac{1-\gamma^5}{2}\right) \nu W_\mu^\dagger \tag{1.16}$$

in a way that, for the only charged current scattering phenomenon $\nu_\mu e^- \to \mu^- \nu_e$ represented in 1.1a, the width $\mathfrak{M}$ will be

$$\begin{aligned} -\imath\mathfrak{M} = \left[\frac{-\imath g}{\sqrt{2}}\overline{u}(\mu)\gamma^\mu \frac{1}{2}(1-\gamma^5)u(\nu_\mu)\right] \frac{\imath(-g_{\mu\nu} + q_\mu q_\nu / M_W^2)}{q^2 - M_W^2} \times \\ \times \left[\frac{-\imath g}{\sqrt{2}}\overline{u}(\nu_e)\gamma^\nu \frac{1}{2}(1-\gamma^5)u(e)\right] \end{aligned} \tag{1.17}$$

that for $q^2 \ll M_W^2$, becomes

$$-\imath\mathfrak{M} = -\frac{\imath g^2}{8M_W^2}\left[\overline{u}(\mu)\gamma^\mu(1-\gamma^5)u(\nu_\mu)\right]\left[\overline{u}(\nu_e)\gamma_\mu(1-\gamma^5)u(e)\right] \tag{1.18}$$

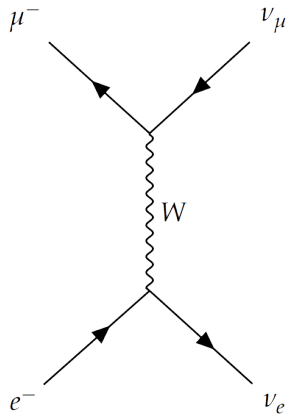

(a) Charged current scattering

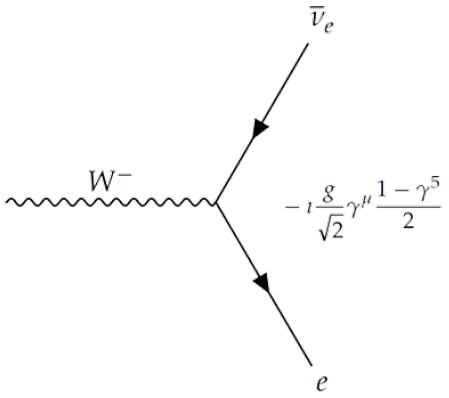

(b) Fundamental charged current vertex

Figure 1.1: Feynman Diagrams

Neutral currents

In neutral currents, bosons γ and Z_0 act the fundamental role in interactions, but they are not eigenvector of $SU(2)_L \otimes U(1)_Y$. In 1.11, a mix between B and W_3 gauge field has been shown.
Moreover, in QED, we know that the vertex with the photon has this kind of expression

$$Q_e \bar{e}^- \gamma_\mu e^- A^\mu$$

that we must find in the Lagrangian of a theory where electromagnetic and weak force should be unified.

$$\begin{aligned} g J^3_\mu W^\mu_3 + \frac{g'}{2} j^Y_\mu B^\mu = &\left(g \cos\vartheta_W J^3_\mu - \frac{g'}{2} \sin\vartheta_W j^Y_\mu \right) Z^\mu \\ &+ \left(g \sin\vartheta_W J^3_\mu + \frac{g'}{2} \cos\vartheta_W j^Y_\mu \right) A^\mu \end{aligned} \tag{1.19}$$

The term A_μ represents the interaction mediated by the photon, so the coefficient must be the same of the electromagnetic one

$$\begin{aligned} g \sin\vartheta_W J^3_\mu + \frac{g'}{2} \cos\vartheta_W j^Y_\mu = e j^{\text{em}}_\mu = e\left(J^3_\mu + \frac{1}{2} j^Y_\mu \right) \\ e = g \sin\vartheta_W \\ e = g' \cos\vartheta_W \\ \tan\vartheta_W = g'/g \end{aligned} \tag{1.20}$$

On the other hand the first term of 1.19 represents the neutral weak current coupling to the Z_μ field.

$$\left[g\cos\vartheta_W J^3_\mu - \frac{g}{2}\frac{\sin^2\vartheta_W}{\cos\vartheta_W}\left(2j^{\text{em}}_\mu - 2J^3_\mu\right)\right]Z^\mu = \frac{g}{\cos\vartheta_W}\underbrace{\left[J^3_\mu - j^{\text{em}}_\mu\sin^2\vartheta_W\right]}_{j^{\text{NC}}_\mu}Z^\mu \tag{1.21}$$

therefore

$$j^{\text{NC}}_\mu = J^3_\mu - j^{\text{em}}_\mu\sin^2\vartheta_W = \overline{\chi}_L\gamma_\mu\frac{\tau_3}{2}\chi_L - \sin^2\vartheta_W\overline{\chi}\gamma_\mu Q\chi$$

Usually this current is written in a way that the left and the right components are distinguishable.

$$\begin{aligned} j^{\text{NC}}_\mu &= \frac{g}{\cos\vartheta_W}\overline{\chi}\gamma_\mu\left[t_3\frac{1-\gamma_5}{2} - Q\sin^2\vartheta_W\right]\chi \\ &= \frac{g}{\cos\vartheta_W}\overline{\chi}\gamma_\mu\left[c^l_L\frac{1-\gamma_5}{2} + c^l_R\frac{1+\gamma_5}{2}\right]\chi \end{aligned}$$

where the coupling costant to the Z field has been added.
In this way, the coefficients of the right component c^l_R and of the left component can be computed

$$\begin{aligned} c^l_L &= t^l_3 - Q_l\sin^2\vartheta_W \\ c^l_R &= -Q_l\sin^2\vartheta_W \end{aligned}$$

A scattering phenomenon that is only neutral current mediated is the diffusion $e\mu \to e\mu$ 1.2. In that case the width $\mathfrak{M}$ is

$$\begin{aligned} -\imath\mathfrak{M} = \left[\frac{-\imath g}{\cos\vartheta_W}\overline{u}(e)\gamma^\mu(\mathbb{P}_{\mathbb{L}}c^e_L + \mathbb{P}_{\mathbb{R}}c^e_R)u(e)\right]\frac{\imath(-g_{\mu\nu} + q_\mu q_\nu/M^2_Z)}{q^2 - M^2_Z}\times \\ \times\left[\frac{-\imath g}{\cos\vartheta_W}\overline{u}(\mu)\gamma^\mu(\mathbb{P}_{\mathbb{L}}c^\mu_L + \mathbb{P}_{\mathbb{R}}c^\mu_R)u(\mu)\right] \end{aligned} \tag{1.22}$$

that for $q \ll M^2_Z$ becomes

$$\begin{aligned} -\imath\mathfrak{M} = \frac{-\imath g^2}{4\cos^2\vartheta_W M^2_Z}\left[\overline{u}(e)\gamma^\mu(\mathbb{P}_{\mathbb{L}}c^e_L + \mathbb{P}_{\mathbb{R}}c^e_R)u(e)\right]\times \\ \times\left[\overline{u}(\mu)\gamma^\mu(\mathbb{P}_{\mathbb{L}}c^\mu_L + \mathbb{P}_{\mathbb{R}}c^\mu_R)u(\mu)\right] \end{aligned} \tag{1.23}$$

1.1.4 Fermions Coupling with Higgs bosons

Field theories had been used with great success in understanding strong and electromagnetic interaction. On contrary both weak and electroweak interaction field theory cannot explain all the experimental evidences discovered in

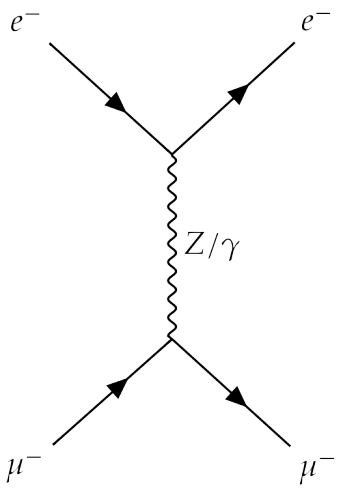

Figure 1.2: $e\mu \to e\mu$ diffusion

the second half of twentieth century.
As a matter of fact a Dirac mass term mixes left and right component in the following way

$$-m\overline{\psi}\psi = -m(\overline{\psi}_L\psi_R + \overline{\psi}_R\psi_L) \tag{1.24}$$

The 1.24 shows that a massive fermion is not invariant under a $SU(2)_L$ transformation, so Dirac mass terms break the simmetry of weak interaction.
1964 PRL symmetry breaking papers proposed related but different approaches to explain how mass could arise in local gauge theories. These paper theorized a field ϕ characterized by a $SU(2)_L$ doublet with a non zero expectation mean value (v).

$$\langle 0|\phi|0\rangle = \frac{1}{\sqrt{2}}\begin{pmatrix}0\\ v\end{pmatrix} \tag{1.25}$$

After spontaneously symmetry breaking, the Higgs doublet in the unitary gauge is

$$\phi(x) = \begin{pmatrix}\phi^+\\ \phi^0\end{pmatrix} = \frac{1}{\sqrt{2}}\begin{pmatrix}0\\ v+h(x)\end{pmatrix}$$

LEPTONS In the Standard Model, left-handed chiral leptons are placed in $SU(2)_L$ doublets with the associated neutrino, while right-handed leptons are placed in $SU(2)_L$ singlets.
In Higgs theory, even the ϕ field is placed in $SU(2)_L$ doublet, so the transformations in this group have these effects

$$\phi \to \phi' = (\mathbb{I} + \imath g_W \boldsymbol{\epsilon}(x)\cdot\mathbf{T})\phi \tag{1.26}$$

$$\overline{\chi}_L \to \overline{\chi}'_L = \overline{\chi}_L(\mathbb{I} - \imath g_W \boldsymbol{\epsilon}(x)\cdot\mathbf{T}) \tag{1.27}$$

Consequently, the combination $\overline{\chi}_L \phi$ is invariant under the $SU(2)_L$ gauge transformations. When combined with a right-handed singlet, $\overline{\chi}_L \phi \chi_R$, it is invariant under $SU(2)_L \odot U(1)_Y$ gauge transformations; as is its Hermitian conjugate $(\overline{\chi}_L \phi \chi_R)^\dagger = (\overline{\chi}_R \phi^\dagger \chi_L)$. Hence, a term in the Lagrangian of the form $-g_f(\overline{\chi}_L \phi \chi_R + \overline{\chi}_R \phi^\dagger \chi_L)$ satisfies the $SU(2)_L \odot U(1)_Y$ gauge symmetry of the Standard Model. For the $\overline{\chi}_L$ doublet containing the electron, this corresponds to

$$\begin{aligned}\mathcal{L}_e &= -g_e \left[\begin{pmatrix} \overline{\nu}_e & \overline{e} \end{pmatrix}_L \begin{pmatrix} \phi^+ \\ \phi^0 \end{pmatrix} e_R + \overline{e}_R \begin{pmatrix} \phi^{+*} \\ \phi^{0*} \end{pmatrix} \begin{pmatrix} \nu_e & e \end{pmatrix}_L \right] \\ &= -\frac{g_e}{\sqrt{2}} v(\overline{e}_L e_R + \overline{e}_R e_L) - \frac{g_e}{\sqrt{2}} h(\overline{e}_L e_R + \overline{e}_R e_L)\end{aligned}$$

where g_e is known as the Yukawa coupling of the electron in the Higgs field. The first term has exactly the form required for the fermion masses, assuming that $g_e = \sqrt{2}\, m_e / v$, but has now been introduced in a gauge invariant way. The second term shows how electron interacts with the Higgs boson.
Feynman diagrams of these two kind of interaction are represented in 1.3.

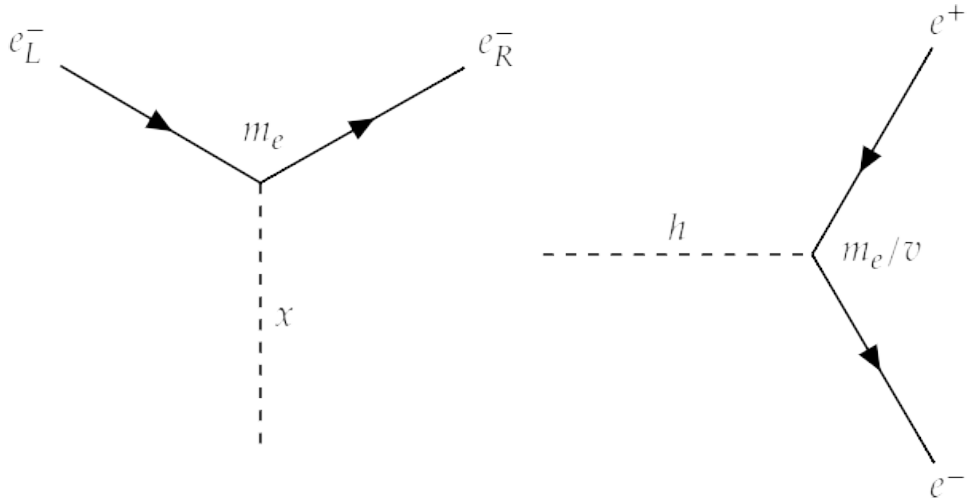

Figure 1.3: Left: the interaction between a massless chiral electron and the non-zero expectation value of the Higgs field.
Right: the interaction vertex for the coupling of the Higgs boson to an electron

QUARKS The same combination of fields $\overline{\chi}_L \phi \chi_R$ can be used to give the mass to quarks too. Because the only non-zero component of the Higgs field is the neutral one, only down-type quarks become massive. This argument was not important for leptons, because in the Standard Model neutrinos are considered massless despite the recent experimental evidences about neutrino masses that

can be considered beyond the SM.
The mechanism to give mass to the up-type quark is achieved by constructing the conjugate doublet ϕ_C

$$\phi_C = -\imath\tau_2\phi = \begin{pmatrix} -\phi^{0*} \\ \phi^- \end{pmatrix}$$

A gauge invariant mass term for the up-type quarks can be constructed from $\overline{\chi}_L\phi_C\chi_R + \overline{\chi}_R\phi_C^\dagger\chi_L$, for example

$$\mathcal{L}_u = g_u \begin{pmatrix} \overline{u} & \overline{d} \end{pmatrix}_L \begin{pmatrix} -\phi^{0*} \\ \phi^- \end{pmatrix} u_R + h.c. \tag{1.28}$$

In this way it is possible to assign a mass for every $SU(2)_L$ eigenstate. Quark mass eigenstates are different from $SU(2)_L$ eigenstate because of their mixing, it is necessary to build a formalism to rotate down-like quark for this mechanism.
Let's write left quark fields:

$$q_{L1} = \begin{pmatrix} u_{L1} \\ d_{L1} \end{pmatrix} \qquad q_{L2} = \begin{pmatrix} u_{L2} \\ d_{L2} \end{pmatrix} \qquad q_{L3} = \begin{pmatrix} u_{L3} \\ d_{L3} \end{pmatrix} \tag{1.29}$$

and right quark singlets:

$$u_{R1} \quad d_{R1} \quad u_{R2} \quad d_{R2} \quad u_{R3} \quad d_{R3} \tag{1.30}$$

In this way it is easier to write the complete Lagrangian for every quark

$$L_{\phi f} = b_{ij}\overline{q}_{Li}\phi d_{Rj} + a_{ij}\overline{q}_{Li}\phi_C u_{Rj} + h.c. \tag{1.31}$$

$$= -\left(1 + \frac{h}{v}\right)\left[\overline{u}_{Li}m^u_{ij}u_{Rj} + \overline{d}_{Li}m^d_{ij}d_{Rj} + h.c.\right] \tag{1.32}$$

in this formalism, different masses have been assigned

$$m^u_{ij} = -\frac{v}{\sqrt{2}}a_{ij} \qquad m^d_{ij} = -\frac{v}{\sqrt{2}}b_{ij}$$

Obviously quark masses must be six, three for m^u_{ij} and three for m^d_{ij}, so these two $3x3$ matrixes must be diagonal. For this purpose, a representation of masses eigenstates will be

$$u_{L\alpha} = (U^u_L)_{\alpha i}u_{Li} \qquad u_{R\alpha} = (U^u_R)_{\alpha i}u_{Ri}$$
$$d_{L\alpha} = (U^d_L)_{\alpha i}d_{Li} \qquad d_{R\alpha} = (U^d_R)_{\alpha i}d_{Ri}$$

To conclude this argument, charged current Lagrangian will be written in this way

$$\mathcal{L}_{CC} = -\frac{g}{\sqrt{2}}\begin{pmatrix} \overline{u}_{Lj} & \overline{d}_{Lj} \end{pmatrix}\gamma^\mu\tau_+ W_\mu \begin{pmatrix} u_{Lj} \\ d_{Lj} \end{pmatrix} + h.c. \tag{1.33}$$

$$= -\frac{g}{\sqrt{2}}\overline{u}_{Lj}\gamma^\mu d_{Lj}W_\mu + h.c. \tag{1.34}$$

$$= -\frac{g}{\sqrt{2}}\overline{u}_{L\alpha}\left[(U^u_L)_{\alpha j}(U^d_L)^\dagger_{\beta j}\right]\gamma^\mu d_{L\beta}W_\mu + h.c. \tag{1.35}$$

a remarkable achievement is that the CKM matrix (previously theorized in another way) is a consequence of Higgs mechanism, in fact

$$V_{\alpha\beta} = \left[(U_L^u)(U_L^d)^\dagger\right]_{\alpha\beta}$$

The next section deals with this mixing matrix because it is fundamental to study flavour physics, the main theoretical argument of this thesis work.

1.1.5 Standard Parametrization of the CKM Matrix

Let us now determine the number of physical parameters in the CKM matrix. For $\mathcal{CPT}$ symmetry to be conserved, the CKM matrix necessarily needs be unitary and hence the matrix elements are correlated. Thus, it can be parametrized by three mixing angles and six complex phases in general, since a unitary matrix has to follow the condition: $VV^\dagger = \mathbb{I}$.
However, five of these phases are non-physical, as they can be absorbed as unobservable parameters into the up-type and down-type quarks, respectively. Note that an overall phase rotation of all quarks does not affect the CKM matrix. The standard parametrization of the CKM matrix reads

$$V_{\text{CKM}} = \begin{pmatrix} 1 & 0 & 0 \\ 0 & c_{23} & s_{23} \\ 0 & -s_{23} & c_{23} \end{pmatrix} \begin{pmatrix} c_{13} & 0 & s_{13}e^{-\imath\delta} \\ 0 & 1 & 0 \\ -s_{13}e^{\imath\delta} & 0 & c_{13} \end{pmatrix} \begin{pmatrix} c_{12} & s_{12} & 0 \\ -s_{12} & c_{12} & 0 \\ 0 & 0 & 1 \end{pmatrix} \tag{1.36}$$

where $s_{ij} = \sin\vartheta_{ij}$ and $c_{ij} = \cos\vartheta_{ij}$; ϑ_{12}, ϑ_{13} and ϑ_{23} are the three angles (real parameters); and δ represents the complex phase. Note that the angle ϑ_{12} corresponds to the Cabibbo angle,ϑ_C, discussed for the case of two quark families and is the largest of the mixing angles. In order for $\mathcal{CP}$ violation to occur in the quark sector, the parameter δ then needs to be unequal to zero. To have a better overview, numerical values are reported

$$s_{12} \approx 0,22 \qquad s_{23} \approx 0,04 \qquad s_{13} \approx 4 \times 10^{-3} \tag{1.37}$$

The CKM matrix hence is close to the unit matrix, with hierarchical off-diagonal elements. Flavour changing transitions are therefore strongly suppressed in the SM. Similarly, also the quark masses are found to follow a hierarchical pattern, spanning five orders of magnitude in size.
It can be beneficial to express the elements of the matrix in terms of an expansion in the comparably small but real parameter $\lambda = \sin\vartheta_{12}$. In addition, three other real parameter A, ρ and η are defined such that

$$A\lambda^2 = \sin\vartheta_{23} \qquad A\lambda^3(\rho - \imath\eta) = \sin\vartheta_{13}e^{-\imath\delta} \tag{1.38}$$

Up to $\mathcal{O}(\lambda^4)$, the CKM matric can then be writtes as

$$V_{CKM} = \begin{pmatrix} 1 - \lambda^2/2 & \lambda & A\lambda^3(\rho - \imath\eta) \\ -\lambda & 1 - \lambda^2/2 & A\lambda^2 \\ A\lambda^3(1 - \rho - \imath\eta) & -A\lambda^2 & 1 \end{pmatrix} \tag{1.39}$$

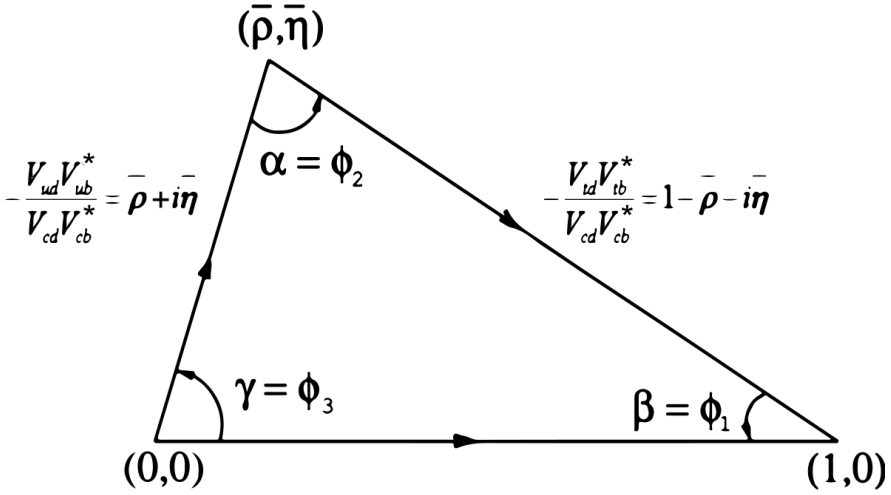

Figure 1.4: Unitary Triangle

This widely used representation is referred to as the Wolfenstein parameterization [17].

1.1.6 The Unitarity Triangle

The unitarity condition of the CKM matrix leads to nine independent equations. The one most relevant to B physics is:

$$V_{ud}^* V_{ub} + V_{cd}^* V_{cb} + V_{td}^* V_{tb} = 0 \tag{1.40}$$

because all the addendi of this sum are $\mathcal{O}(\lambda^3)$, while the other 8 conditions have different orders in λ.
In order to form the *unitarity triangle (UT)*, we divide this equation by $V_{cd}V_{cb}^*$ (assuming this like a real parameter)

$$1 + \frac{V_{ud}^* V_{ub}}{V_{cd} V_{cb}^*} + \frac{V_{td}^* V_{tb}}{V_{cd} V_{cb}^*} = 0 \tag{1.41}$$

In figure 1.4 the complex sum 1.41 is shown where

$$\begin{aligned} \overline{\rho} &= \rho\left(1 - \frac{\lambda^2}{2}\right) \\ \overline{\eta} &= \eta\left(1 - \frac{\lambda^2}{2}\right) \end{aligned} \tag{1.42}$$

Depicting the rescaled Unitarity Triangle in the $(\overline{\rho};\overline{\eta})$ plane, the lengths of the two complex sides are

$$R_b = \sqrt{\overline{\rho}^2 + \overline{\eta}^2} = \frac{1 - \lambda^2/2}{\lambda}\left|\frac{V_{ub}}{V_{cb}}\right|, \qquad R_t = \sqrt{(1-\overline{\rho})^2 + \overline{\eta}^2} = \frac{1}{\lambda}\left|\frac{V_{td}}{V_{cb}}\right| \tag{1.43}$$

and with some approximations, the phases of CKM matrix can be written as:

$$V_{td} = |V_{td}|e^{-\imath\beta} \qquad \text{e} \qquad V_{ub} = |V_{ub}|e^{\imath\gamma} \tag{1.44}$$

Unitary triangle angles can be measured by the study of B mesons:

- $\sin 2\beta$ from $B_d \to J/\psi K_S, \phi K_S$
- $\sin 2\alpha$ from $B_d \to D\pi$ and $B_S \to D_s K$
- γ from $B_d \to \pi\pi, DK$.

In the chapter 3, these kind of measure will be explained.
First, the CKM matrix and the UT have to be determined from tree levelcharged current decays as accurately as possible. As this determination is independentof potential New Physics (NP) contributions, the result can be used as input for precise SM predictions of rare, loop-induced FCNC processes. These predictions are then to be compared withthe data, which – in case of a discrepancy – would yield an unambiguous sign of a NP contribution to the decay in question. Clearly, in order to be able to claim a NP discovery in flavour violating observables, a solid understanding of the SM contribution and its uncertainties is mandatory.

2 BELLE II EXPERIMENT

In this chapter the main features of the SuperKEKB accelerator are described. The machine upgrade and the physics goals have required a profound transformation to the detector, which had to overcome several technological challenges. A general picture of the experiment is presented, from the subdetectors architecture to experiment's goals, giving more details on the topics which will be useful for the rest of the thesis.
In an electron-positron collider the most efficient way to produce B mesons is to tune the energy to the $\Upsilon(4S)$, the lightest strong resonance with a mass sufficient to decay in b-flavoured mesons ($B^0\overline{B}^0$ or B^+B^- pairs). Indeed the beauty meson threshold is at $2m(B) \approx 10.56\,\text{GeV}$ and $m_{\Upsilon(4S)} \approx 10.58\,\text{GeV}$.
In an e^+e^- collider, the study of rare or forbidden decays is ideal, because of the lower track multiplicity compared with the hadron machines (like LHCb), e.g. an average $\Upsilon(4S)$ event is characterized only by 11 charged tracks, between pions, kaons and leptons. Moreover the trigger efficiency is higher in this kind of experiments is much higher. In this thesis the studied phenomenoun is $B \to \tau\nu$ and the detection of the τ is much easier in a leptonic collision. In this kind of interaction there are numerous known control samples with which a background (and the signal) can be simulated. The table 2.1 reports the cross sections of the main phenomena in an e^+e^- collision at this energy. The precisely known center-of-mass energy and the excellent detector hermeticity are indispensable to perform "missing mass" analyses, where the existence of new particles can be inferred via energy/momentum conservation. The branching fractions for the decay of the $\Upsilon(4S)$ into BB pair is over 96%. The pair of B

$e^+e^- \to$	Cross Section (nb)
$\Upsilon(4S)$	1.110
$c\bar{c}$	1.30
$u\bar{u}$	1.61
$d\bar{d}$	0.40
$s\bar{s}$	0.38
$\tau^-\tau^+(\gamma)$	0.919
$\mu^-\mu^+(\gamma)$	1.148
$e^-e^+(\gamma)$	300

Table 2.1: e^+e^- main processes

mesons results entangled in the decay and the $\Upsilon(4S)$ in unflavoured, which implies that from the knowledge of the characteristics of one B it is possible to assign the related features to the second B too.
Due to the small mass difference between the $\Upsilon(4S)$ and the two B mesons, the latter are produced with little momenta, so their mean path is relatively short ($\tau_B = 1.64\,\text{ps}$). Since one of the goals of Belle II is the measure of the $\mathcal{T}$ violation via the difference of the decay lengths between the entangled Bs, the electron-positron beams are asymmetric, resulting in a center-of-mass frame boosted with respect to the laboratory frame. In the section 2.1, all the characteristics of the accelerator are explained.

2.1 THE SUPERKEKB ACCELERATOR

The Belle II experiment is installed in the interaction point of the SuperKEKB accelerator in Tsukuba, Japan. The machine is currently the only e^+e^- running B-factory in the world with a design luminosity[1] of $8 \times 10^{35}\,\text{cm}^{-2}\text{s}^{-1}$ [13]. The essential elements in the increase of the luminosity are a reduction in the the beam size at the collision point by a factor of 20 and an increase in the currents by a factor of 2 compared to the KEKB values, where Belle (the predecessor of Belle II) was installed. This is known as a "nano-beam" scheme, and was invented by P. Raimondi for the Italian super B-factory [7]. The reduction of the luminous volume size to about 5% with respect to the predecessor KEKB, combined with doubling of beam currents, is expected to yield a factor 40 gain in intensity (figure 2.1). These characteristics bring to the result of the Lorentz

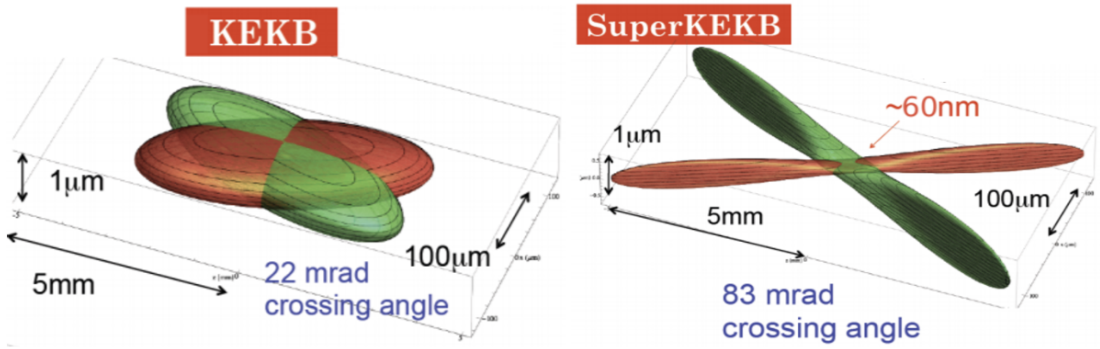

Figure 2.1: Two-dimensional sketch of the nano-beam mechanism implemented in SuperKEKB (right) compared with the previous KEKB collision scheme (left)

1 The luminosity is the ratio between the number of event and the cross section of that given event. Its measure unit is $\text{cm}^{-2}\text{s}^{-1}$ because the number of events is usually measured like a temporal rate dN/dt

	LER(e^+)	HER(e^-)	
Energy	4,000	7,007	GeV
Half crossing angle	41,5	41,5	mrad
Horizontal emittance	3,2	4,6	nm
Emittance ratio	0,27	0,25	%
β functions at IP(x/y)	32/0,27	25/0,30	mm
Beam currents	3,6	2,6	A
Beam-beam parameter	0,0881	0,0807	/

Table 2.2: SuperKEKB beam characteristics

boost factor

$$\beta\gamma = \frac{|\vec{p}_{e^+} + \vec{p}_{e^-}|}{\sqrt{s}} \approx 0,28 \tag{2.1}$$

that is around two-thirds of that at KEKB. This condition is advantageous for analyses with neutrinos in the final state that require good detector hermeticity, but leads also to less separation between the B vertices, in fact the spatial resolution of the Vertex Tracker has to be very precise. SuperKEKB is designed

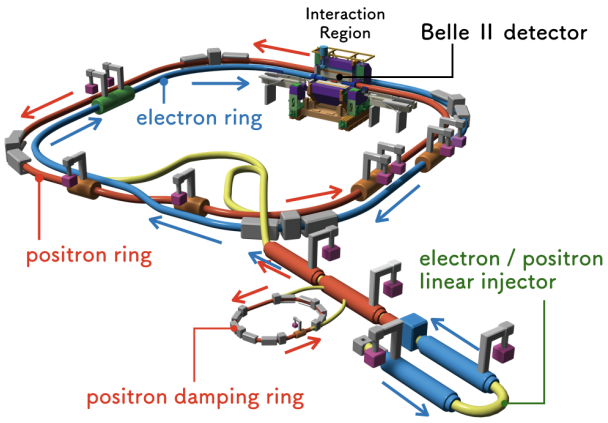

Figure 2.2: SuperKEKB accelerator complex with the upgraded and the new components

to deliver collisions corresponding to 50 ab^{-1} of integrated luminosity by 2030, corresponding $\approx 5.3 \times 10^{10}$ of BB pairs.
Electrons are produced via photoelectric effect by illuminating a cold cathode with a pulsed laser, then accelerated to 7 GeV with a linear accelerator and injected in the High Energy Ring (HER). Positrons are produced by colliding electrons on tungsten; they are first injected in a damping ring to reduce their emittance, which is the average spread of particles in position and momentum phase-space (a small emittance corresponds to particles confined in a small

region and having a similar momentum), then accelerated to 4 GeV with the linear accelerator and injected in the Low Energy Ring (LER). When the circulating beams are sufficiently intense, they are brought to collision in the Interaction Point (IR).

2.1.1 Beam-Induced Background

The characteristics of the beams lead to a not negligible background. The cross section of the background phenomena have been studied and precise predictions are also based on simulated SuperKEKB data.
The background sources are the following:

1. **Touschek effect**: an intra-bunch Coulomb scattering process which deviates the particle energies from nominal values. The scattered particles propagate around the accelerating ring and finally are lost at the beam pipe inner wall, producing a shower. In order to reduce this effect in the SuperKEKB sub-detectors, in the final section of the beam pipe, collimators and metal shields are located;

2. **Beam gas scattering**: the beam could interact with residual gas molecules in the beam pipe by Bremsstrahlung or elastic scattering. The countermeasures used for Touschek background are efficient also for beam-gas background;

3. **Radiative Bhabha scattering**: the photons could interact with the SuperKEKB magnets producing neutrons by photo-nuclear resonance mechanism. In order to reduce this effect, a neutron shield has benne placed close to the detector;

4. **QED processes**: e^+e^- collision could lead to many QED processes, e.g. $e^+e^- \rightarrow e^+e^-e^+e^-$ and the generated particles might spiral inside the detector. Moreover, the accelerating process generate hopelessly synchrotron radiation (from few keV to tens of keV). However, the beam pipe shape is designed to avoid synchrotron radiation photons pass through the detector. Moreover, the inner surface of beryllium beam pipe is gold plated to absorb scattered photons. These precautions should completely suppress the synchrotron radiation background.

2.2 OVERVIEW OF THE BELLE II DETECTOR

The Belle II experimental setup is a major upgrade of its predecessor, Belle, and targets more ambitious physics goals. It is a system of multiple subdetectors, each optimized to reconstruct some specific features arranged asymmetrically

in concentric layers forming an approximately cylindrical layout around the collision point of the SuperKEKB accelerator. While it is located in the same experimental hall and has a similar design to its predecessor, most of its detectors are new or considerably upgraded. A more efficient charged hadron identification is implemented for increased separation of final-state charged hadrons, reduction of backgrounds, and improved flavor-tagging; a better resolution in the reconstruction of the decay positions (vertices) of long lived particles is achieved, to enhance background suppression and sensitivity in measurements of decay-time dependent quantities; a more hermetic acceptance is achieved thanks to the smaller boost of the center of mass of the collision. These improvements are achieved through technologies designed to sustain the side-effects of higher SuperKEKB instantaneous luminosity.
The main subsystems are shown in Figure 2.3. They are detailed in next sections and can be broadly classified as follows:

- **Detectors for charged particle tracking**: silicon pixel and strip detectors close to the beam pipe and a wire drift chamber, all immersed in a 1.5 T magnetic field parallel to the beam axis, are used for reconstruction of charged-particle trajectories (tracks).
- **Detectors for particle identification**: Cherenkov radiators, an electromagnetic calorimeter, and scintillators for muon and long-lived neutral hadrons achieve particle identification.
- **Trigger system**: a two-stage trigger is designed to acquire interesting events at the high rates expected at design luminosities.

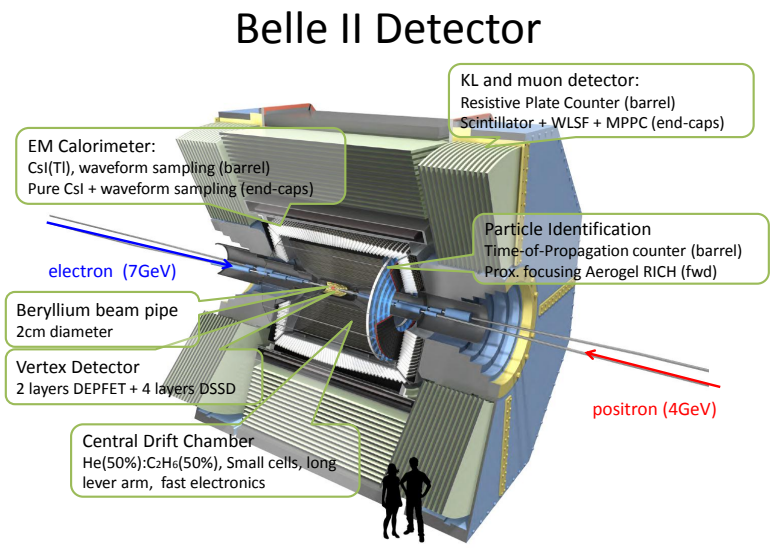

Figure 2.3: Top view of the Belle II detector.

2.3 TRACKING DETECTORS

The innermost detectors are used for the tracking of charged-particle reconstruction. Effective track reconstruction is of great importance since flavor-physics final states are mostly composed of charged particles and analyses rely strongly on precise measurements of their momenta and the decay positions of their long-lived parent particles, in order to separate signal and background thanks to invariant-mass reconstructed by kinematics variables. Moreover, information on the decay time is key for measurements of $\mathcal{CP}$-violating asymmetries involving mixing, because an entangled state composed by a BB pair leads to a same path between the two meson before the decay. To simplify pattern recognition, tracks are first reconstructed in the outer tracking volume, and are then extrapolated into the innermost detector to define coarse regions of interest around their expected intersection points in the inner active layers. If a measurement point is found in the region of interest, the corresponding event is included in the pattern recognition algorithm, otherwise it is not considered.

2.3.1 Silicon-pixel vertexing detector

The innermost detector is a pixel vertexing detector (PXD).
PXD sensors are based on depleted electric field-effect transistor technology. Incident particles generate electron-hole pairs in the depleted region, and thus induce a current. Sensors are 75 µm thick.

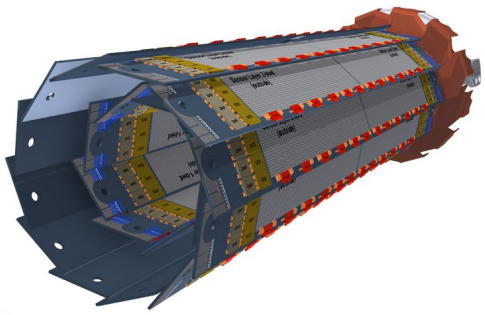

Figure 2.4: Scheme of the PXD detector geometry

The PXD consists of two sets of rectangular layers arranged around the beam pipe with a cylindrical simmetry, at 14 and 22 mm radii and it has a longitudinal dimension of 174 mm at the radius of the outer layer. It comprises around 8 million pixels and the polar acceptance ranges from 17° to 150°.

2.3.2 Silicon-microstrip vertexing detector

A little outer the PXD there is the SVD, a silicon detector with the goal to reconstruct decay vertices and charged-particle tracks at high spatial resolution [3].
SVD uses double-sided silicon strips. Each sensor is a classice photodiode, hence traversing charged particles ionize the silicon, freeing electron-hole pairs that drift due to the electric field, and induce a signal in the electrodes. The fine segmentation of SVD sensors reduces the dead time of the detector, to deal with the high expected rates.

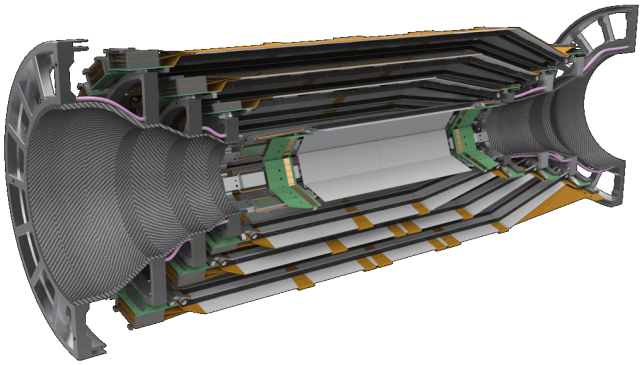

Figure 2.5: Exploded view of a SVD detector half

As shown in Figure 2.5, SVD has a cylindrical asymmetric geometry that mirrors the asymmetry due to the center-of-mass boost. The polar acceptance ranges from 17° to 150°. SVD is radially structured into four concentric layers at 39, 80, 104, and 135 mm, composed by, respectively, 7, 10, 12, and 16 independently readout modules. Sensors are 300 µm-thick, and the separation between adjacent sensing strips ranges from 50 µm to 240 µm. Hence, the spatial resolution varies with the polar angle. Since the charge associated with an incident particle is usually distributed among several strips, position resolution is improved by interpolation.

2.3.3 Central drift chamber

The CDC is a drift chamber, hence its objective is to identify particles by measuring their specific-ionization energy-loss. It samples charged-particle trajectories at large radii, thus providing trigger signals for events containing charged particles. The CDC has a hollow cylindrical geometry with radii between 16 cm and 113 cm. The chamber is composed of 14336 sense wires, divided in 56 layers, immersed in a gaseous mixture of 50% He and 50% C_2H_6, while 42240 aluminum wires shape the electric field. The azimuthal acceptance ranges from 17° to 180°.
The single hit has a about 100 µm spatial resolution and the energy resolution

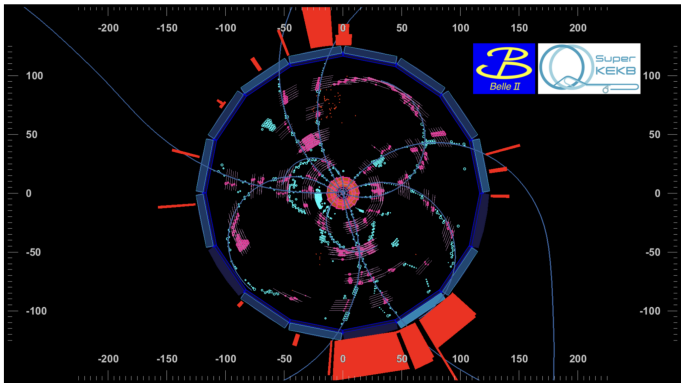

Figure 2.6: Example of event display of a typical hadronic event at Belle II. Curved tracks are reconstructed in the CDC

is 11.9% for an incident angle of 90°. Figure 2.6 shows a reconstructed cosmic-ray track in the CDC. The transverse momentum resolution is $\sigma(p_T)/p_T^2 \approx 0,5\%/\text{GeV}$.

2.3.4 Particle-identification detectors

Charged particle identification in the Belle II experiment is characterized by by two detectors: the time of propagation counter (TOP) and the aerogel ring-imaging Cherenkov counter (ARICH). Their principle is the same: the Cherenkov light. Particle-identification information is also provided by the electromagnetic calorimeter (ECL) and the K_L^0 and muon detector (KLM).

2.3.5 Time of propagation counter

The TOP counter is located in the barrel region. It measures the time of propagation of the photons produced by charged particles with Cherenkov effect. A three-dimensional image of the cone is reconstructed using the correlation between hits positions in the $x-y$ plane and time of propagation. The TOP consists of 16 quartz bars mounted on the barrel at 1,2 m radius from the interaction point. Each bar is a photon radiator and has three main components (Fig. 2.7): a long section where Cherenkov radiation happens; a spherical mirror mounted on the forward end, which focuses the light; and a prism, mounted on the backward end of the bar, which collects and guides the photons to a photomultiplier.

The polar angular acceptance ranges from 31° to 128°. The single-photon time resolution is about 100 ps, providing a good separation of pions and kaons with momentum between 0,4 GeV and 4 GeV (kaon identification efficiency is about 95%, pion fake rate is about 10%). This time resolution is achieved with a photo-multiplier specially developed for this purpose.

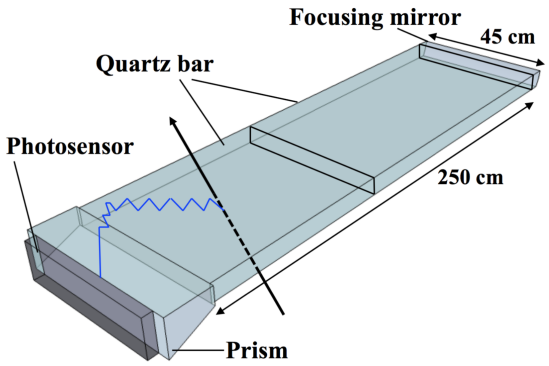

Figure 2.7: Sketch of a TOP quartz bar

2.3.6 Aerogel ring-imaging Cherenkov

Kaon-Pion separation is also provided by ARICH counter, which measures the Cherenkov ring produced by the passage of charged particles through a radiator. The ARICH provides not only discrimination between pions and kaons, but also discrimination between pions, muons, and electrons below 1 GeV. When charged particles pass through the aerogel radiator, Cherenkov photons are produced; they propagate in a expansion volume where they form a ring on a photo-diodes surface, developed the measure of the position. As shown in Figure 2.8, two aerogel radiators with different refraction indexes are used to increase the number of generated photons without degrading the Cherenkov-angle resolution [13].

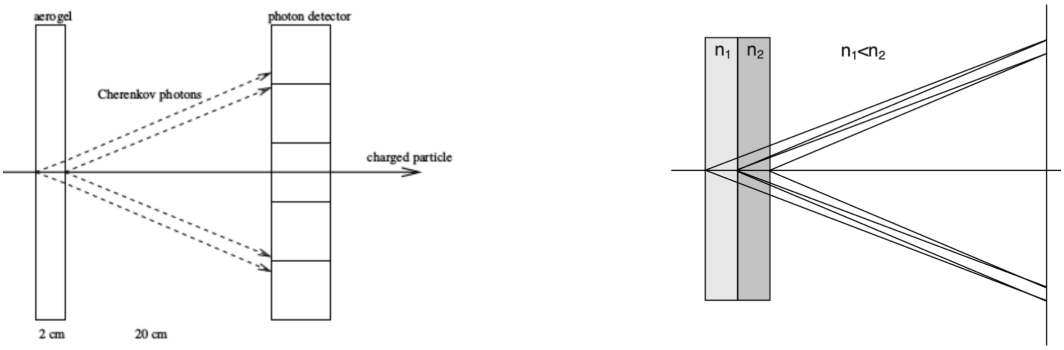

Figure 2.8: Scheme of the ARICH counter

The ARICH is composed of 420 modules for photon detection arranged in seven layers extending from 0,41 to 1,14 m radii, and by 248 aerogel tiles placed on the detector endcaps. The polar angular acceptance ranges from 14° to 30°. The observed ARICH performances allows for a 5σ separation between 0,4 and 4 GeV momenta kaons and pions, and a 4σ separation between pions, muons and electrons slower (momenta smaller than 1 GeV).

2.3.7 Electromagnetic calorimeter

The electromagnetic calorimeter (ECL) is the end of the path for photons and electrons. This characteristic allows the ECL to detect photons over a wide energy range as well as to identify electrons and separate them from hadrons. These cluster are related a posteriori with the CDC tracks. The ECL is a highly-segmented array of thallium-doped and cesium iodide crystals. To improve the probability to emit a photon in the visible, Thallium impurities are added to create other energy level, in which the electrons can "jump". The scintillation light is then collected by phototubes. The $CsI(Tl)$ crystals offer a good time resolution, which reduces the contamination of beam-background photons, which are not in time with the collision products. In the ECL, photons and electrons are identified through their kinematics, shower shapes and timing information, as they have different (in shape and magnitude) energy losses with respect to charged hadrons. To separate electrons from photons, information from tracking detectors is correlated with the ECL signal. The ECL consists of a 3-m-long barrel section with an inner radius of 1,25 m. The polar angle coverage ranges from 12,4° to 155,1°. The energy resolution ranges from σ_E/E = 4% at 100 MeV to σ_E/E = 1.6% at 8 GeV. The observed resolution for the reconstructed π_0 mass is 8 MeV. The ECL also allows for determining luminosity by measuring the Bhabha scattering rate and using its precisely known cross-section.

2.3.8 K_L^0 and muon detection system

The KLM detects muons and neutral particles, because most of the particles get absorbed before the last step of the Belle II experimental setup. It is made of alternating iron plates and active detector elements, this kind of detector is called "sampling calorimeter", because has active and inactive components. Iron elements act also as magnetic flux returns for the tracking solenoid. In the inner layers, the active material is scintillator, while in the outer layers are RPC (resistive plate chambers), with a gas mixture filling the space between electrodes. When particles traverse the KLM, they produce charges that are collected by applying an appropriate voltage. The barrel section of the detector covers 45° to 125° in polar angle. The endcaps cover 20° to 45° and 125° to 155°. Design reconstruction efficiency exceeds 80% for muons with momentum greater than 1 GeV and K_L^0 with momentum greater than 3 GeV.

2.3.9 Trigger System

The Belle II trigger system covers a very important role to reject background events and accept event of interest during data taking. The bunch crossing time is about 4 ns and it is much faster than the detectors signal collection

time, so the beam can be considered continuous. Anyway, at full luminosity, the expected event rate is about 50 kHz, and over than 90% of these events are Bhabha scattering or 2γ QED processes (the Bhabha cross section is about 300 times greater than the resonance).
Despite BB events are characterized by a higher charged track multiplicity with respect to others events, this variable can not be used in the trigger because τ and low multiplicity events would be discarded too. The required trigger must have instead an efficiency close to 100% for BB events, since B forbidden or rare decays are one of the main studied physics phenomena. Some efficiency degradation is allowed to suppress the Bhabha and 2γ QED backgrounds. The trigger rate must be below 30 kHz, the maximum acquisition frequency of DAQ, and the trigger must provide time information with a precision below 10 ns to exploit the potential of the Belle II sub-detectors.
The Belle II trigger is composed in two main stages: a hardware trigger or Level 1 trigger (L1) and a software trigger or High Level Trigger (HLT). The first one removes most of the background events with the help of the faster sub-detectors (frequency higher than 30 kHz), while the second one refine the selection with a more exhaustive analysis and reduce the event rate from L1 trigger to a storable rate of 10 kHz.

3 B MESON PHYSICS

While the previous section introduced the underlying concepts, we now apply them to the B-meson system. The study of different decay channels of charged and neutral B-mesons represents the major part of the physics program of Belle II. Examining the branching ratios of these decays can be used to determine the sides of the unitarity triangle, whereas measurements of $\mathcal{CP}$ violation yield the angles of the triangle.
We begin by discussing the production of charged and neutral B-mesons in Section 3.1. This is followed by the phenomenological description of the mixing of neutral B-mesons and their time-dependent oscillations in Section 3.2.

3.1 PRODUCTION

As reported above, SuperKEKB mainly operate at a center-of-mass energy of $\sqrt{s} = 10.58\,\text{GeV}$ which correspond to the mass of the $\Upsilon(4S)$ resonance. Generally, the various Υ resonances are meson bound states of $b\overline{b}$. A key role among these resonances is assumed by the $\Upsilon(4S)$ since it is the first excited state with a sufficiently large mass to decay into a pair of B-mesons. The production and subsequent decay of such an $\Upsilon(4S)$ is illustrated in Figure 3.1.
Particle Data Group [18] reports that for a percentage greater the 96%, $\Upsilon(4S)$ decays in $B\overline{B}$, in particular The charged and neutral B-meson pairs are essentially created at rest in the center-of-mass system of the $\Upsilon(4S)$, because

$$\Delta m = m(\Upsilon(4S)) - 2m(B^+) \approx m(\Upsilon(4S)) - 2m(B^0) \approx 22\,\text{GeV}$$

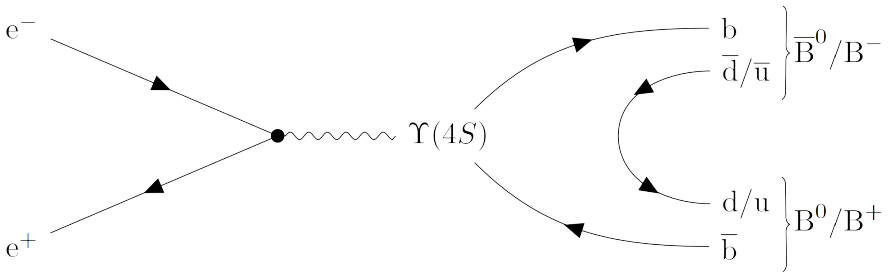

Figure 3.1: Leading-order Feynman diagram for the production of $\Upsilon(4S)$ resonances in e^+e^- collisions

Decay Mode	Branching Ratio
$\Upsilon(4S) \to B^0(\bar{b}d)\overline{B}^0(b\bar{d})$	48,6%
$\Upsilon(4S) \to B^+(\bar{b}u)B^-(b\bar{u})$	51,4%

Table 3.1: $\Upsilon(4S)$ decays

.
This further implies that the relatively short lived B-mesons ($\tau = 1.519\,\text{ps}$) have low velocities and propagate only a short distance before decay, for this reason, SuperKEKB has different energies for the electrons' and positrons' beams, in particular the center of mass frame has a Lorentz boost (compared to the laboratory frame) with $\beta\gamma = 0,28$. Important for their further evolution is the fact that they are produced in quantum correlated states.
The charged and neutral B-mesons either decay fully hadronic to lighter mesons or semi-leptonic to pairs of leptons and lighter mesons. They are important probes for the study of QCD and $\mathcal{CP}$ violation phenomena and have various rare decays which are sensitive to NP.

3.2 OSCILLATIONS

The previous section described how B-mesons are produced in e^+e^- resonance. The Standard Model foresees that weak interaction must take place between flavour and/or $\mathcal{CP}$ eigenstates, but it does not foresee how particles propagate, in particular a particle propagate as its mass eigenstate, that does not always match with flavour eigenstate.
In this thesis, neutral B-mesons will explained, but this argument can be applied (with different numeric values) for K, D, B_s.
At $t = 0$, B^0 and $\overline{B}^0$ can overlap themselves and can stay in a state called ψ.

$$|\psi(t)\rangle = \alpha(t)\left|P^0\right\rangle + \beta(t)\left|\overline{P}^0\right\rangle \tag{3.1}$$

and the evolution of this state follows Schroedinger equation

$$\imath\frac{\mathrm{d}}{\mathrm{d}t}\begin{pmatrix}\alpha\\ \beta\end{pmatrix} = \mathcal{H}\begin{pmatrix}\alpha\\ \beta\end{pmatrix} = \begin{pmatrix}H_{11} & H_{12}\\ H_{21} & H_{22}\end{pmatrix}\begin{pmatrix}\alpha\\ \beta\end{pmatrix} \tag{3.2}$$

where $\mathcal{H}$ is a not-Hermitian operator 2x2 given by the mass matrix M and the decay matrix Γ. Since there are a large number of B-meson decay modes, of which only a few are common to both the B^0 and $\overline{B}^0$, and the contribution to

the Hamiltonian of from the interference between the decays of the B^0 and $\overline{B}^0$ can be neglected, $\Gamma_{12} = \Gamma_{21}^* \approx 0$.

$$\mathcal{H} \approx \begin{pmatrix} M - \frac{\imath}{2}\Gamma & M_{12} \\ M_{12}^* & M - \frac{\imath}{2}\Gamma \end{pmatrix} \tag{3.3}$$

where M_{12} is due to the box diagrams reported in 3.2. The eigenvalues of 3.3, which determine the masses and lifetimes of the physical states, are

$$\lambda_H = m_H + \Gamma_H \frac{\imath}{2} \approx M + |M_{12}| - \Gamma \frac{\imath}{2} \tag{3.4}$$

$$\lambda_L = m_L + \Gamma_L \frac{\imath}{2} \approx M - |M_{12}| - \Gamma \frac{\imath}{2} \tag{3.5}$$

leading to a heavier state B_H and a lighter state B_L.
The corresponding physical eigenstates of the Hamiltonian are

$$|B_L\rangle = p\left|B^0\right\rangle + q\left|\overline{B}^0\right\rangle \quad \text{and} \quad |B_L\rangle = p\left|B^0\right\rangle - q\left|\overline{B}^0\right\rangle \tag{3.6}$$

the coefficients p and q are complex numbers with the normalization $|p|^2 + |q|^2 = 1$,, for which the ratio is given by

$$\frac{q}{p} = -\sqrt{\frac{M_{12}^* - \Gamma_{12}^* \frac{\imath}{2}}{M_{12} - \Gamma_{12} \frac{\imath}{2}}} \tag{3.7}$$

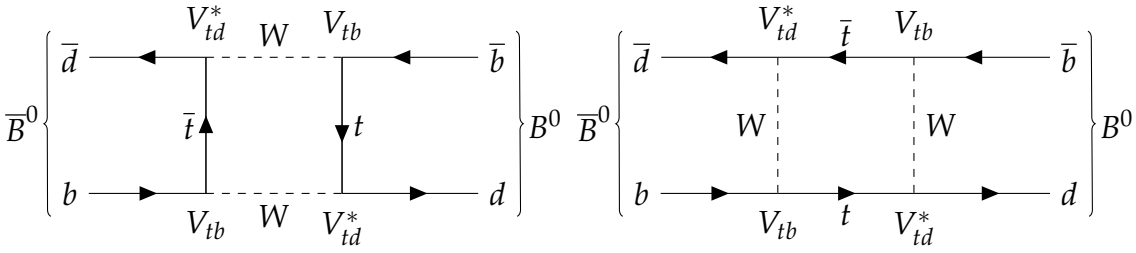

Figure 3.2: Leading-order Feynman diagrams or box diagrams for $B^0 \leftrightarrow \overline{B}^0$ mixing

3.2.1 $\mathcal{CP}$ violation in the B-meson system

Through these phenomena, experiments like Belle and BaBar have measured and established that $\mathcal{CP}$ violation can be observed as three distinct effects:

1. direct $\mathcal{CP}$ violation in decay such that $\Gamma(B \to f) \neq \Gamma(\overline{B} \to \overline{f})$;
   A decay amplitude is given by the matrix element $\left\langle f \middle| \mathcal{H} \middle| B^0 \right\rangle = \Gamma_f$. The $\mathcal{CP}$ coniugate of this decay can be obtained in this way:

$$\Gamma_f = \left\langle f \middle| \mathcal{H} \middle| B^0 \right\rangle = \left\langle f \middle| (\mathcal{CP})^\dagger (\mathcal{CP}) \mathcal{H} (\mathcal{CP})^\dagger (\mathcal{CP}) \middle| B^0 \right\rangle \tag{3.8}$$

$$= \left\langle \overline{f} \middle| \mathcal{H} \middle| \overline{B}^0 \right\rangle e^{\imath(\phi_{\mathcal{CP}} - \phi_{\mathcal{CP}f})} = \overline{A}_f e^{\imath(\phi_{\mathcal{CP}} - \phi_{\mathcal{CP}f})} \tag{3.9}$$

   where $\phi_{\mathcal{CP}}$ and $\phi_{\mathcal{CP}f}$ are the phases given by $\mathcal{CP}$ on the states $\left|B^0\right\rangle$ and $|f\rangle$. The violating occurs where $\left|\overline{A}/A\right| \neq 1$.

2. $\mathcal{CP}$ violation in the mixing of neutral mesons;
   The violation occurs when $|p/q| \neq 1$ and it is quantizable with the parameter ϵ

$$\epsilon = \frac{p-q}{p+q}$$

3. $\mathcal{CP}$ violation in the interference between decays to a common final state f with or without mixing, for example $B^0 \to f$ and $B^0 \to \overline{B}^0 \to f$. Again a phase convention independent quantity exists which is given by

$$\lambda_f = \frac{q}{p}\frac{\overline{A}_f}{A_f}$$

   It implies a $\mathcal{CP}$ violation if $\lambda_f \neq \pm 1$. This means that even if $|q/p| = 1$ and $\overline{A}_f/A_f = 1$, there could be a violation if $\mathrm{Im}\{\lambda\} \neq 0$.

3.3 B MESON PHYSICS: LEPTONIC DECAYS

This thesis had the main goal to measure the Branching Ratio of a purely leptonic B decay, in particular, $B \to \tau\nu$. The Standard Model provides a very precise theoretical prediction of the Branching Ratio, for these reason a precise measure of this quantity could be an important stress of the hypothesized model. The calculation gives:

$$\mathcal{BR}(B \to \ell\nu) = \frac{G_F m_B m_\ell^2}{8\pi}\left[1 - \frac{m_\ell^2}{m_B^2}\right]^2 f_B^2 |V_{ub}|^2 \tau_B \tag{3.10}$$

where G_F is the Fermi constant, m_B and m_ℓ are the B^+ meson and the lepton masses, respectively, and τ_B is the B^+ lifetime.
Using the lattice QCD calculation of $f_B = (189 \pm 4)$ MeV, and the *BABAR* measurement of $|V_{ub}|$ from charmless semileptonic B exclusive decay, the predicted SM value of the Branching Ratio is $\mathcal{BR} = (0.62 \pm 0.12) \times 10^{-4}$. If we use the *BABAR* measurement of $|V_{ub}|$ from inclusive charmless semileptonic B decays,

the prediction is $\mathcal{BR} = (1.18 \pm 0.16) \times 10^{-4}$ [14].
These values are the highest Branching fraction of a purely leptonic decay of B meson, that is the τ mode. As a matter of fact, in equation 3.10 we can note that

$$\mathcal{BR}_\tau : \mathcal{BR}_\mu : \mathcal{BR}_e \approx (4 \times 10^6) : (4 \times 10^4) : 1 \tag{3.11}$$

i.e. only an upper limit for the Branching ratio of $\mu\nu$ mode can be measured, while the $e\nu$ decay is detectable only if new physics greatly enhances its decay rate.
The process is sensitive to possible extensions of the SM. For instance, in two-Higgs doublet models (2HDM) [11], it can be mediated by a charged Higgs boson. A branching fraction measurement can, therefore, also be used to constrain the parameter space of new physics models 3.3.

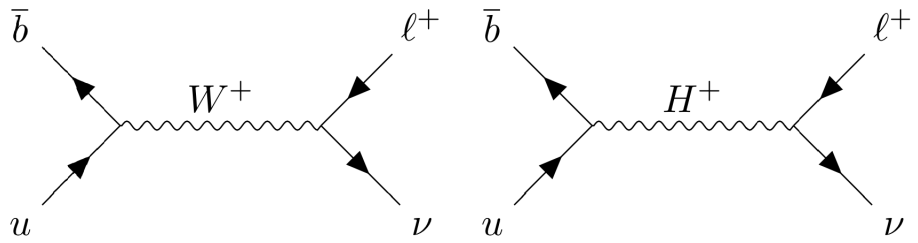

Figure 3.3: Feynman diagrams of purely leptonic B^+ decays, mediated by a charged weak boson(left) or a charged Higgs as predicted in new physics models (right)

Combining the measurements by Belle and BaBar, the average is given as $(1.06 \pm 0.19) \times 10^{-4}$ [14][2], which has over 5σ significance. The last value reported on the PDG review [18] is $(1.09 \pm 0.24) \times 10^{-4}$; both are consistent with the prediction at 2σ.
In the SM context, the observation of $B \to \tau\nu$ provides an experimental value of f_B (considering as known $|V_{ub}|$). Viceversa, if f_B is calculated precisely from QCD lattice, the branching ratio measurement could bring to an indirect measurement of $|V_{ub}|$.
Even if the purely leptonic decay offers a clean signature to extract the signal events from the backgrounds, the helicity suppression makes the decay in the muon and electron channels harder to study.
Moreover, in 3.3, there is an other possible Feynman diagram in which the gauge boson is a charged Higgs. If this channel exists the Branching Ratio must be corrected by a factor proportional to the expectation value of the charged Higgs field, that in SM is equal to o *a priori*.
In [11], all the theoric calculations are presented, in this thesis I will report only the final result, i.e.

$$\mathcal{BR}(B \to \tau\nu) = \mathcal{BR}_{SM}\left(1 - \frac{M_{B^+}^2}{m_{H^+}^2}\tan^2\beta\right) \tag{3.12}$$

Decay Mode	Branching Ratio (%)
$\tau \to \mu\nu\nu$	17,39
$\tau \to e\nu\nu$	17,82
$\tau \to \pi\nu$	10,81
$\tau \to \pi\pi^0\nu$	25,49
$\tau \to \pi\pi^0\pi^0\nu$	9,30
$\tau \to \pi\pi\pi\nu$	8,98

Table 3.2: Main τ decay modes

where $\tan\beta = v_2/v_1$, and $v_{1,2}$ are the vacumm expectation values of a doublet in the Higgs field.
Comparing the measured value of the branching ratio and the SM prediction, it is possible to exclude regions in the $(m_{H^+}; \tan\beta)$ plane.

3.4 τ DECAYS

Due to its mass ($m_\tau \approx 1.77\,\text{GeV}$), the τ is the only lepton that decays in hadrons. The main τ-decay modes are

- leptonic decays, i.e. $\tau \to \ell\nu\nu$ (figure 3.4a);
- hadronic decays, i.e. $\tau \to \pi\nu$, $\tau \to \rho\nu$ and $\tau \to a_1\nu$, where $\rho \to \pi\pi$ and $a_1 \to \pi\pi\pi$ immediately(figure 3.4b).

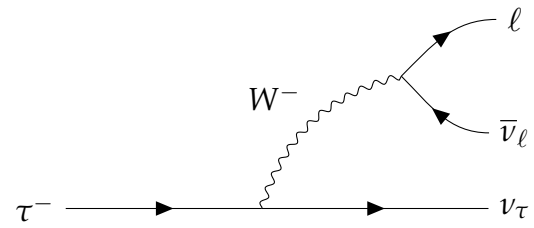

(a) Feynman diagrams of a τ leptonic decay

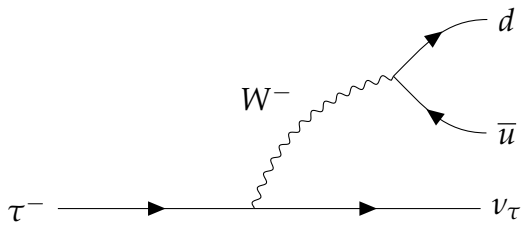

(b) Feynman diagrams of a τ hadronic decay

Figure 3.4: Feynman diagrams of a τ decay

In the table 3.2 all the main τ decays are reported [18]

4 SEARCH FOR $B \to \tau\nu$ DECAY

The aim of this chapter is to describe the sensitivity of the Belle II experiment to the search for $B \to \tau\nu$ decays, studying Monte Carlo simulated samples of physics events produced in e^+e^- collisions at the center of mass energy of $\sqrt{s} = 10.58\,\text{GeV}$ and analyzing collision data collected in 2019 and first part of 2020 (corresponding to an integrated luminosity of $62.8\,\text{fb}^{-1}$) .
First, a description of the dataset used is given, followed by the discussion of the strategy implemented in order to reject the most abundant backgrounds. The main backgrounds could be divided in three parts:

- Continuum Background: $e^+e^- \to q\overline{q}$ or $e^+e^- \to \ell\ell$ (non-resonant);
- Charged B: $e^+e^- \to \Upsilon(4S) \to B^+B^-$;
- Neutral B: $e^+e^- \to \Upsilon(4S) \to B\overline{B}$;

.
The $B \to \tau\nu$ signal is searched for using the 1-prong decays of τ lepton: $\tau \to e\nu\nu$, $\tau \to \mu\nu\nu$, $\tau \to \pi\nu$, $\tau \to \rho\nu$ with $\rho \to \pi\pi^0$.
The algorithm used to reconstruct the B_{tag} is described (Full Event Intepretation) and subsequently, the signal selection and its optimization.
In the last part of this chapter, the $B \to \tau\nu$ Branching Ratio is measured assuming an increasing luminosity from $100\,\text{fb}^{-1}$ to $1000\,\text{fb}^{-1}$, using a likelihood minimization alghorithm, in order to estimate the luminosity at which the 5σ observation is reached.

4.1 COMPUTING ENVIRONMENT

The following thesis was carried out using the *Root* package, a data analysis software developed by CERN.
The software was written in C++, but it also uses other programming languages, such as Python and R.
The data collected by the Belle II experiment or produced in the Monte Carlo simulations are organized in data structures called *Trees*, that contain, for each event, variables describing the quantities of physical interest.

4.2 DATASET AND MC SAMPLES

Data were preliminarly organized into 9 files, 8 containing the Monte Carlo Simulation of the most abundant physics processes and the last is the Belle II experimental data. The simulated categories of events have been reported in Table 4.1.

Event Type	Equivalent luminosity (fb^{-1})	Class
$e^+e^- \to \Upsilon(4S) \to B^+B^- \to \tau\nu X$	325 203	Signal
$e^+e^- \to \Upsilon(4S) \to B^+B^- \not\to \tau\nu X$	955	Background
$e^+e^- \to \Upsilon(4S) \to B^0\overline{B}^0$	953	Background
$e^+e^- \to u\bar{u}$	1000	Background
$e^+e^- \to d\bar{d}$	1000	Background
$e^+e^- \to c\bar{c}$	1000	Background
$e^+e^- \to s\bar{s}$	1000	Background
$e^+e^- \to \tau^+\tau^-$	1000	Background

Table 4.1: MonteCarlo Sample

To study the agreement of the MC simulation with experimental data (excluding the signal region), each MC sample is normalized to $L = 62.8\,\text{fb}^{-1}$, corresponding to the integrated luminosity of data collected in 2019 and the first part of 2020.

4.2.1 Full Event Interpretation

The Full Event Interpretation (FEI) is a tagging algorithm developed within the Belle II experiment, and it is the upgrade of the Full Reconstruction algorithm used at Belle. B factories operate on the $\Upsilon(4S)$ resonance, which decays in two B mesons (charged or neutral) about 96% of the times. Conceptually, the event is divided into three sides:

1. The tag-side containing the tracks and clusters compatible with an arbitrary B_{tag} meson decay.
2. The signal-side containing the tracks and clusters compatible with the assumed signal B_{sig} decay of interest, e.g. $B \to \tau\nu$;
3. The remaining tracks and clusters from objects not associated with either the B_{tag} or the B_{sig} are included in the *Rest of Event* (ROE).

Figure 4.1 depicts this situation. This method is applicable to a wide range of B-decays with a minimum amount of detectable information, like our $B \to \tau\nu$ analysis or no detectable information $B^0 \to \overline{\nu}\nu$ in the final state.
The FEI provides information on:

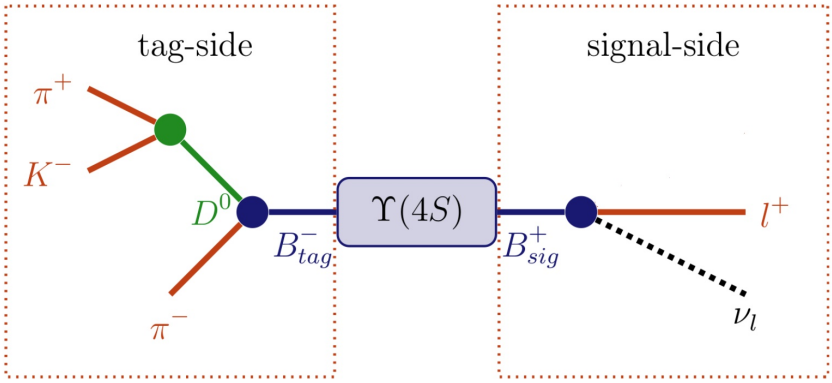

Figure 4.1: (Left) a common tag-side decay and (right) the signal-side decay $B \to \tau^+\nu$ investigated in this thesis

- The event-type: charged or neutral B mesons;
- The decay vertex;
- The four-momentum of the B_{tag} and consequently the B_{sig};
- Clusters and tracks details: assigned to the signal or to the tagging B or Rest of Event.

The FEI provides three types of tags: hadronic, semileptonic and inclusive. The hadronic tagging reconstructs the candidates' kinematics through purely hadronic decays and the tagged sample is the purest. The efficiency in selecting B_{tag} in off the order of 0.1%.
The semileptonic tagging reconstructs semileptonic B decays with at least one neutrino in the final state and has a higher tagging efficiency, but a lower purity than the hadronic tag.
Finally, the inclusive tagging combines the four-momenta of all particles in the rest of the event of the signal-side B candidate (that must be known *a priori*). The achieved tagging efficiency is usually one order of magnitude above the hadronic and semileptonic tagging. Yet the decay topology is not explicitly reconstructed and cannot be used to discard wrong candidates. In consequence, this methods suffers from a high background and the final sample is very impure.
The advantages and disadvantages of the different approaches are visualized in Figure 4.2.
The basic idea of the FEI is to reconstruct individual particle decay channels, which occur in the decay chain of the B meson, in a hierarchical manner. For each unique decay channel of a particle, a Multivariate Classifier (MVC) is trained using simulated events.
The algorithm starts with the information given by the detectors and begins the training of the MVC by reconstructing all the possible decay chains. Every

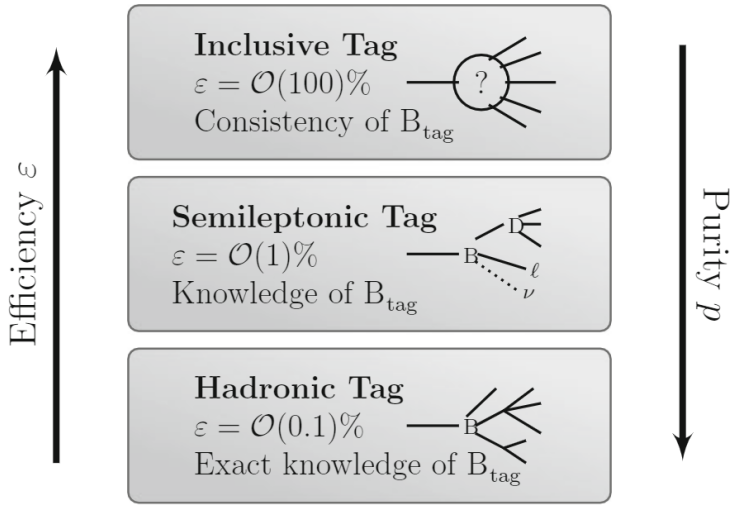

Figure 4.2: Overview of the three tagging algorithms

chain has a hierarchy (Figure 4.3) and, consequently, an associated probability. There is a enormous number of possible combinations of chains and it is unfeasible to handle all possible B meson candidates from all possible combination. For this reason FEI apply Machine Learning methods to preprocessing and postprocessing every layer of its Neural Network.
FEI is trained on MC and subsequently applied to collision data and it is part of BASF2 software package [4] [12].
The MVC combines all information about a candidate into a single value, called signal-probability (*SigProb*). The final output of the FEI to the user contains four particle lists: B^+, hadronic; B^+, semileptonic; B^0, hadronic; B^0, semileptonic.
In this analysis a hadronic tagging method is exploited.
In the case that multiple candidates are reconstructed in the event the one with the highest *SigProb* is chosen.
A *loose* pre-selection is applied to reconstructed B_{tag}, based on the quality of reconstruction. It is based on M_{bc}, the beam constrained B candidate mass, derived from the beam energy ($\sqrt{s}$) and reconstructed B momentum (p_B); ΔE, the difference between the energy of B_{tag} and the expected energy (from the beam); *SigProb*, the FEI alghorithm output. The chosen cuts are:

- $M_{bc} = \sqrt{s/4 - p_B^2} > 5.24\,\text{GeV}$;
- $|\Delta E| = |E_B - \sqrt{s}/2| < 200\,\text{MeV}$;
- $SigProb > 0.001$;

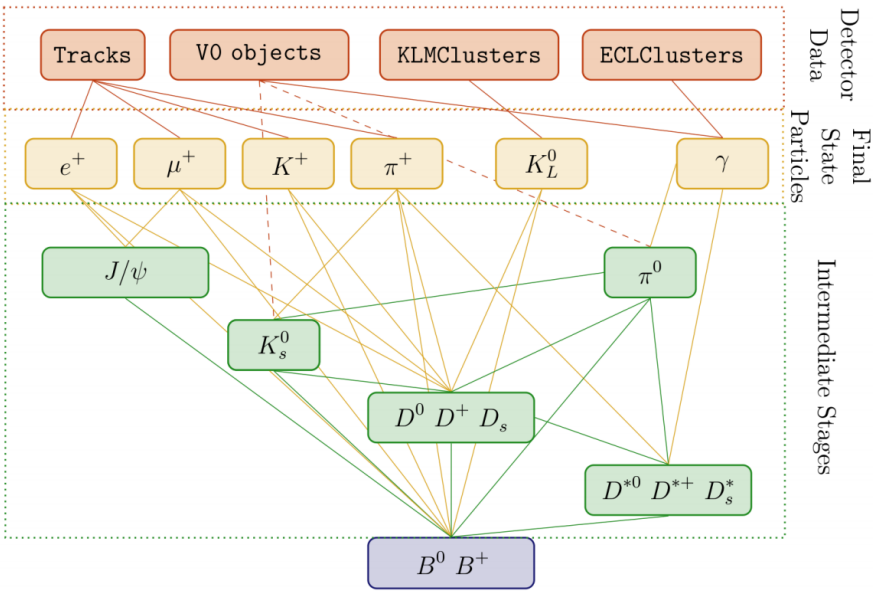

Figure 4.3: Schematic overview of the FEI

4.3 SIGNAL EVENTS SELECTION

After B_{tag} reconstruction, the properties of the remaining particles in the event (B_{sig}) are compared to those expected for signal and background. The requirement is that all remaining particles in the event after removing B_{tag} daughters are consistent with the decay products of $B \to \tau\nu$.
Several features of the $B \to \tau\nu$ decay are exploited in this analysis. In each studied τ decay there is only one charged particle in the final state (e, μ, π and ρ) and only one charged track is visible (e, μ and π). The presence of neutrinos in final state implies a large missing energy. The rest of event (ROE) (much more populated in background events) is exploited to separate signal and background.
The charged particle identification of the signal track (PID) relies on likelihood based selectors: the information from the detector systems, i.e. specific ionization ($\mathrm{d}E/\mathrm{d}x$) from the SVD and the CDC, E/p from ECL and measurements from TOP, ARICH and KLM are analyzed independently to determine a likelihood for each charged particle hypothesis (electron, muon, pion, kaon, proton and deuteron). The likelihoods from each detector are used to construct a combined likelihood ratio:

$$\mathcal{L}_r = \frac{\mathcal{L}(\text{particle})}{\mathcal{L}(e) + \mathcal{L}(\mu) + \mathcal{L}(\pi) + L(K) + L(p) + L(d)} \tag{4.1}$$

Due to the different kinematic characteristics of each decay, the analysis has been divided in four channels as shown in Table 4.2.
The selected categories all together correspond to approximately 71.5% of all τ decays.

Decay mode	BR
$\tau \to e\nu\nu$	17.82 %
$\tau \to \mu\nu\nu$	17.39 %
$\tau \to \pi\nu$	10.82 %
$\tau \to \rho\nu \to \pi\pi^0\nu$	25.49 %

Table 4.2: τ decay modes

The track classification is based on the likelihood function in Eq. 4.1. In this analysis only $\mathcal{L}_e$ and $\mathcal{L}_\mu$ have been used, since the τ hadronic decay have been recognized by negating the leptonic request. The following selection requirement have been chosen:

- Electron mode: Prob($\mathcal{L}_e$) > 0.9;
- Muon mode: Prob($\mathcal{L}_\mu$) > 0.9;
- Pion Mode: Prob($\mathcal{L}_e$) < 0.9 AND Prob($\mathcal{L}_e$) < 0.9;

An event characterized by a pion track could be associated to both $\tau \to \pi\nu$ and $\tau \to \rho\nu$. The ρ channel is identified by the presence of two photons with an invariant mass consistent to π^0 mass and a total invariant mass $\sqrt{\left(p_\pi + p_\gamma^{(1)} + p_\gamma^{(2)}\right)^2} \approx m_\rho$ [1], consistent to a ρ decay. The following criteria have been chosen:

$$120\,\text{MeV} < m_{\gamma\gamma} < 150\,\text{MeV}$$
$$620\,\text{MeV} < m_{\gamma\gamma\pi} < 920\,\text{MeV}$$

If these requirements are not fulfilled, the candidate is selected as π channel.

The following variables have been studied:

- M_{bc}: the beam constrained B candidate mass calculated as

$$M_{bc} = \sqrt{E_{beam}^{*2} - \left|\mathbf{p}_B^{*2}\right|^2} = \sqrt{\frac{s}{4} - p_B^2}$$

- *SigProb:* the output of the B_{tag} algorithm. In order to show the effect of this variable, Figure 4.6 shows M_{bc} distributions in different intervals of *SigProb*.
- $R2$: For a collection of N particles with momenta p_i, the l^{th} order Fox-Wolfram moment H_l is defined as

$$H_l = \sum_{i,j}^{N} |p_i|\,|p_j|\,P_l(\cos\theta_{i,j})$$

1 p_π and p_γ are four-momenta, so the square is the Lorentz-invariant $p_\mu p^\mu$

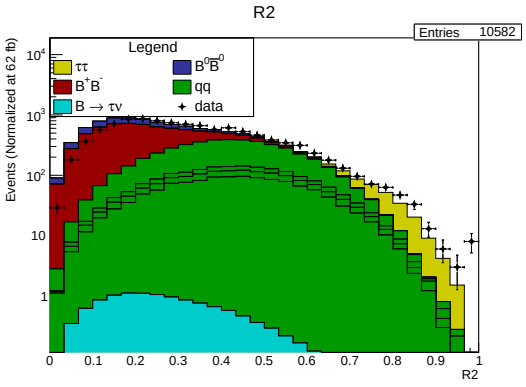

(a) $R2$ distributions

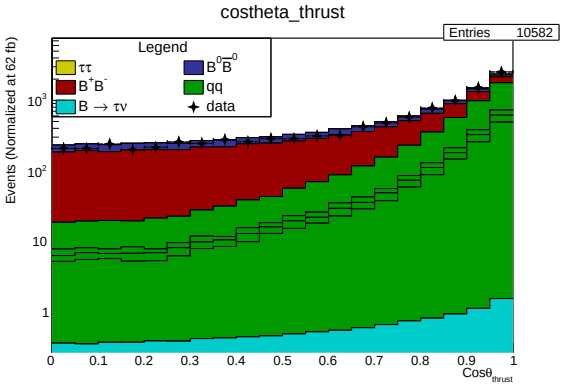

(b) $\cos\theta_{\text{thrust.}}$ distributions

Figure 4.4: Geometric topology of signal and background events

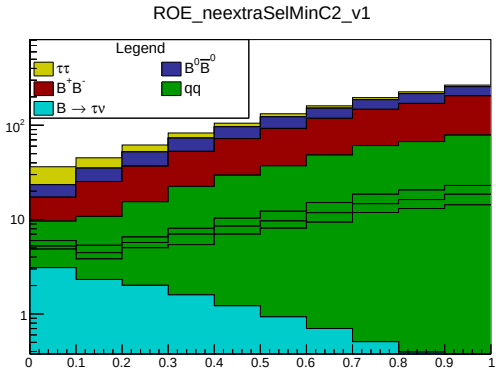

(a) E_{ECL} distribution for e

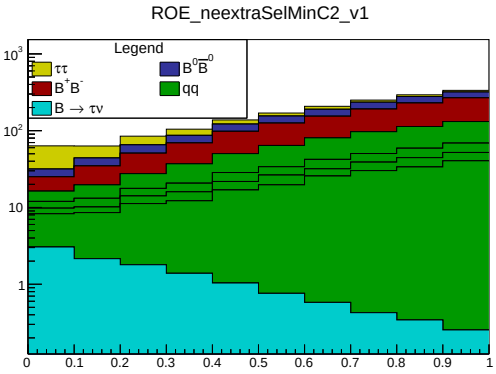

(b) E_{ECL} distribution for μ

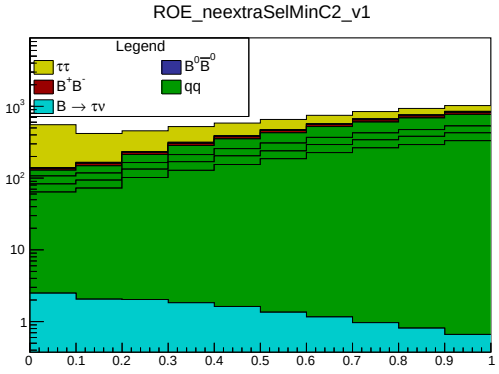

(c) E_{ECL} distribution for π

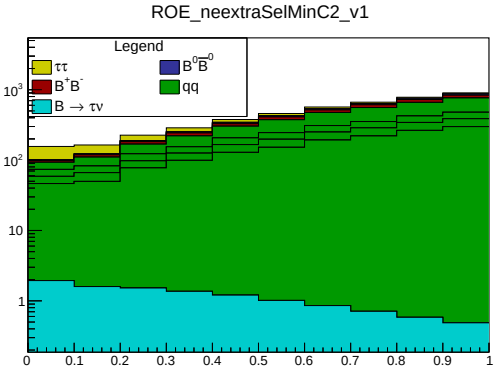

(d) E_{ECL} distribution for ρ

Figure 4.5: E_{ECL} distributions

- $\cos\theta_{\text{thrust.}}$: is the angle between the thrust axis of the momenta of the B candidate decay final state particles, and the thrust axis of the ROE (all evaluated in the $\Upsilon(4S)$ rest frame). It separates events with spherical symmetry, as BB events, presenting a flat distribution, from $q\bar{q}$, $\tau^+\tau^-$ and low multiplicity events with back to back topology, and, therefore, peaking at 1; the Figure 4.4b shows its distribution. where $\theta_{i,j}$ is the angle between p_i and p_j, and P_l is the l^{th} order Legendre polynomial. R2 is the ratio between H_2 and H_0 and separates BB event from the continuum background. In the Figure 4.4a, the $R2$ distribution is shown.

- p^{μ}_{miss}: is the missing quadrimomentum, computed as the difference between the quadrimomentum of the beams and reconstructed particles' quadrimomentum;

- ΔE: is the difference (in the center of mass frame) between the energy of B_{tag} and the beam energy;

- E_{ECL}: is the energy deposited in the calorimeter by objects not associated with either B_{tag} or B_{sig}. This is the most discriminant variable and it will be used to extract the signal from backgrounds, Figure 4.5 shows the E_{ECL} distributions for each channel;

- p^{μ}_{trk}: the quadrimomentum of the charged track (electron, muon or pion);

- $p^{\mu}_{\text{candidate}}$: the τ reconstructed decay products (electron, muon, pion or ρ);

- E_{γ}: the reconstructed energy of the photons from π^0 decay (it is used only in the ρ channel);

In order to reduce contamination from continuum background events (mainly $e^+e^- \rightarrow q\bar{q}$), the following topological variables have been considered: normalised second Fox-Wolfram moments ($R2$) and $\cos\theta_{\text{thrust.}}$.
These different geometric distributions could be exploited to model the continuum component in the signal region, performing a bin-by-bin subtraction of the non-continuum contributions extracted from real data in the continuum enriched region; to check that this procedure is feasible, a comparison of the distributions from the continuum MC of continuum enriched and signal regions is performed. To define continuum and enriched regions, $\cos\theta_{\text{thrust.}} > 0.9$ has been used and the corrispondent signal region is obtained by negating that requirement.
A different continuum enriched region has been checked, using $R2 \gtrless 0.5$ (the signal region is obtained by negating that requirement).
From inspecting Figure 4.7 is evident that the two shapes are not equivalent and the procedure is not feasible.

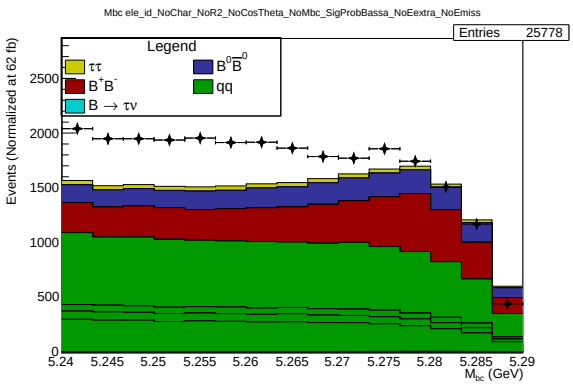

(a) $0.001 < SigProb < 0.01$

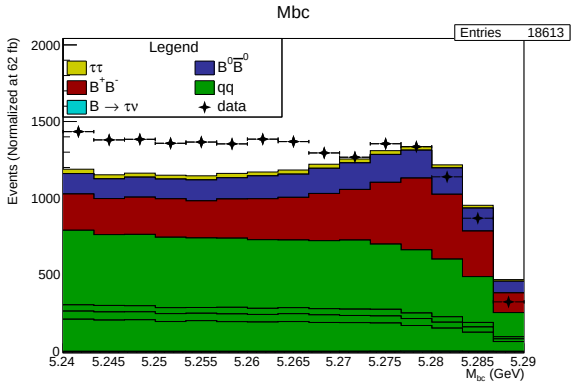

(b) $0.01 < SigProb < 0.1$

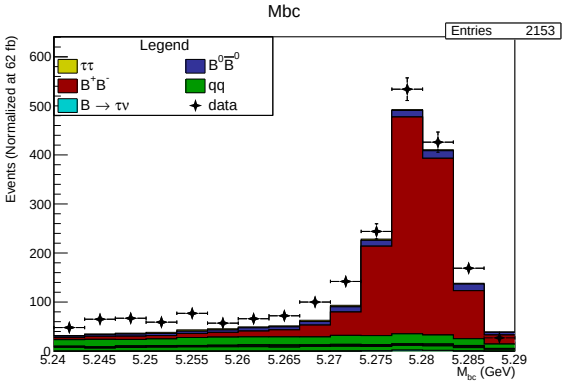

(c) $SigProb > 0.1$

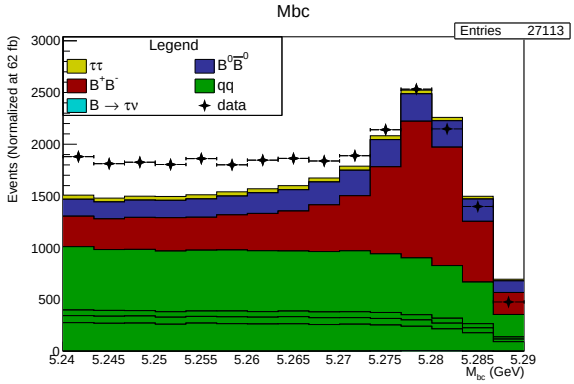

(d) $SigProb > 0.001$

Figure 4.6: Plots of M_{bc} for electrons with the loose preselection. The data-MC discrepancy is due to the imperfect description of continuum events by Monte Carlo simulation

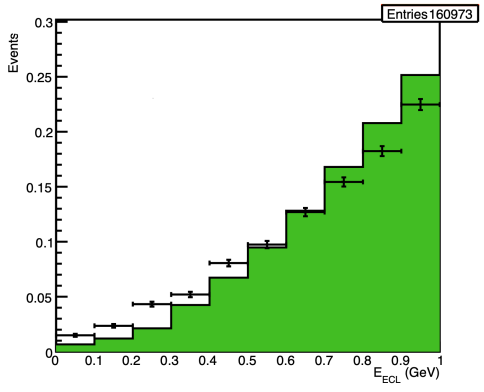

(a) E_{ECL} with $\cos\theta_{\text{thrust.}} < 0.9$ (green) and $\cos\theta_{\text{thrust.}} > 0.9$(points) (normalized at 1)

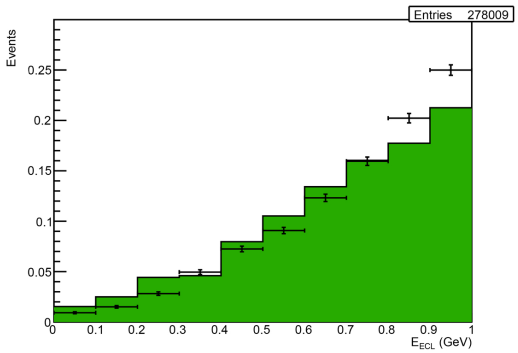

(b) E_{ECL} with $R2 < 0.5$ (green) and $R2 > 0.5$(points) (normalized at 1)

Figure 4.7: Comparison of the MC distributions of continuum background.

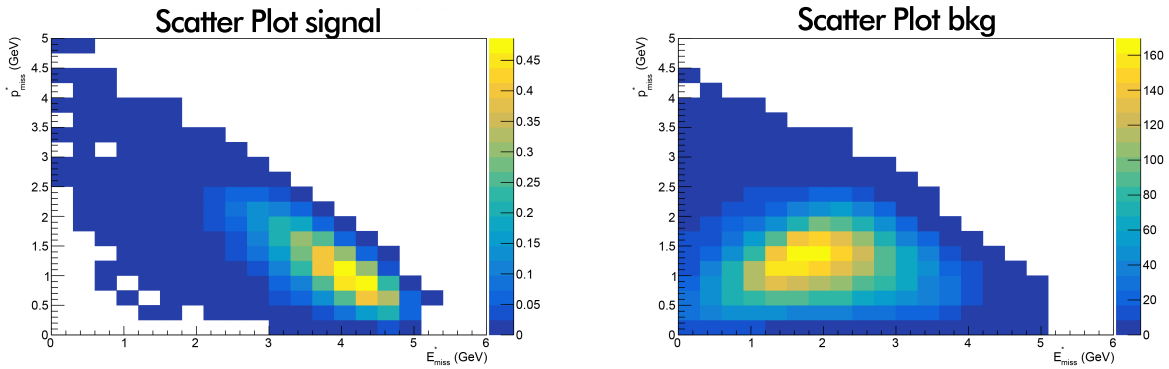

(a) Scatter Plot E_{miss} vs p_{miss} for signal

(b) Scatter Plot E_{miss} vs p_{miss} for all the background

Figure 4.8: Scatter Plot

The E_{ECL} distributions, as shown in Figure 4.5, have been plotted since this will be the most relevant variable in the last part of the analysis. In fact, the best way to discriminate the $B \to \tau\nu$ signal from the background is the extra energy in the electromagnetic calorimeter. For signal events, E_{ECL} should be either zero or a small value deriving from beam background hits and split-offs coming from imperfect reconstruction. Instead, most of background events are distributed toward higher E_{ECL} values because of the higher neutral multiplicity of backgrounds.
In addition to the topological features and differences between signal and background events, other powerful constrains come from the decay kinematics.
The missing momentum is mainly discriminant in leptonic τ decays, due to the presence of three neutrinos in the final state. The best discriminating power has been achieved with a specific linear combination of p^{μ}_{miss} components: $E_{\text{miss}} + p_{\text{miss}}$ (in this thesis natural units are used, $\hbar = c = 1$). The Figure 4.8 shows E_{miss} vs p_{miss} for signal and background events.
The momentum of the visible τ decay products, that in the case of $\tau \to \ell\nu\nu$ and $\tau \to \pi\nu$ decays is the charged track, while it is the sum of the charged track and the photons momenta in $\tau \to \rho\nu \to \pi\pi^0\nu$, is a good discriminant variable for hadronic τ decays.
Two body decay kinematics of $\pi\nu$ and $\rho\nu$ implies a large reconstructed momentum (p_{cand}), on contrary background events are characterized by a low momentum single tracks because of B decay multiplicity.
In Figure 4.9, the distributions of the p_{cand} in the hadronic decays and $E_{\text{miss}} + p_{\text{miss}}$ in the leptonic decays are reported.
Correction factors have been applied to MC simulations in order to take into account the different efficiencies of PID selections measured in data with respect to MC for the electron and muon modes[2][9]. Moreover, the electron and muon

2 Those correction have been studied and provided by the Belle II collaboration with specific studies of experimental data control samples

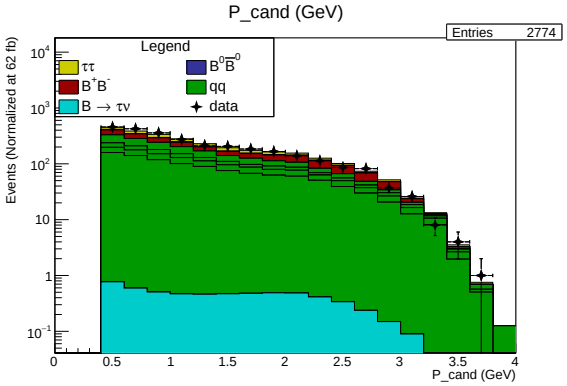

(a) Momentum of π from $\pi\nu$

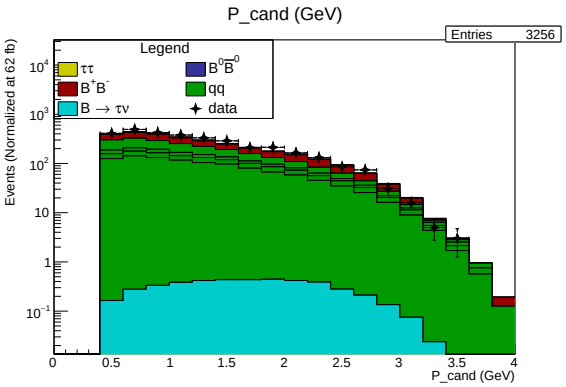

(b) Momentum of ρ from $\rho\nu$: background

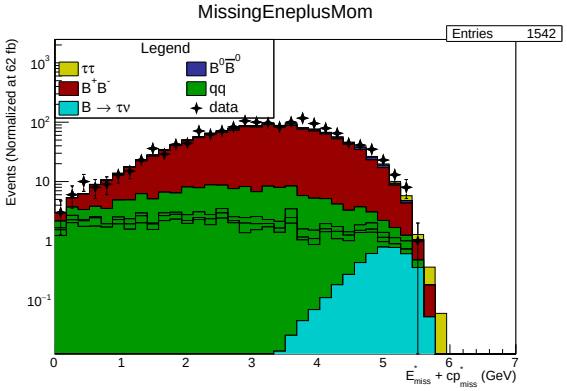

(c) $E_{\text{miss}} + p_{\text{miss}}$ from $e\nu\nu$: signal

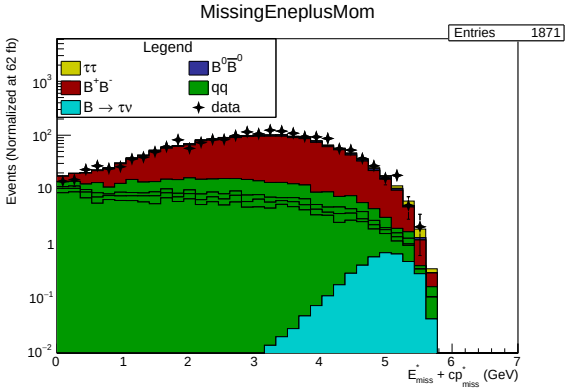

(d) $E_{\text{miss}} + p_{\text{miss}}$ from $\mu\nu\nu$: background

Figure 4.9: Plots of the hadronic momentum and leptonic missing energy

momenta and polar angles have been restricted to the phase space regions where the corrections are available, i.e. $p_{\text{track}} > 0.4\,\text{GeV}$ and $0.56 < \theta < 2.71$. In Figure 4.10 plots of p_{track} before and after the correction have been reported.

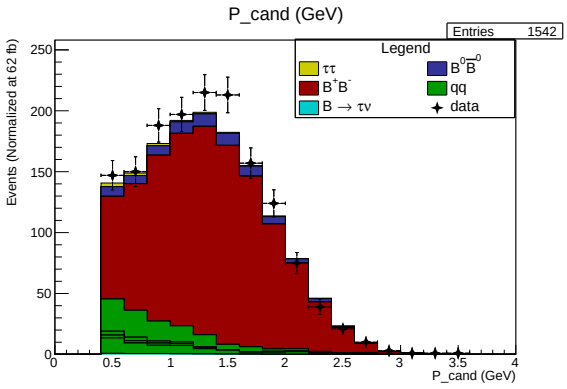

(a) p_{cand} before the correction (electron)

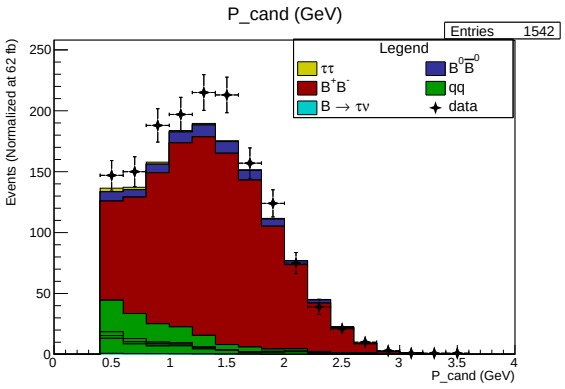

(b) p_{cand} after the correction (electron)

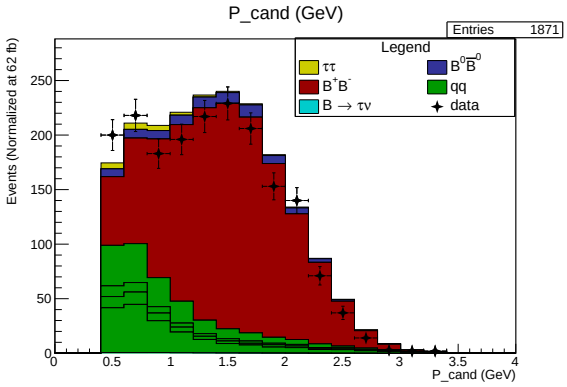

(c) p_{cand} before the correction (muon)

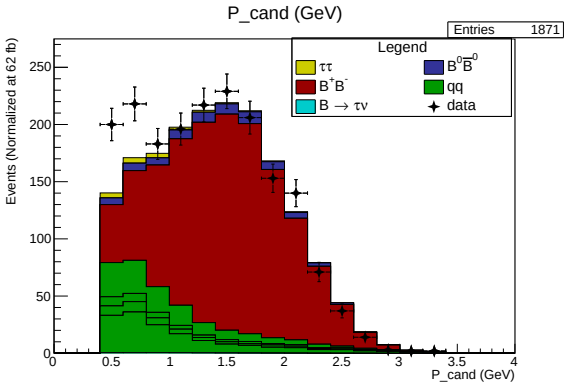

(d) p_{cand} after the correction (muon)

Figure 4.10: Momentum correction factor applied to p_{track}

4.3.1 Signal Selection Optimization

In this thesis, two optimization methods of the signal selection have been implemented:

1. Significance method by event counting: the objective is to maximize the significance $Z = s/\sqrt{b}$: in this section this method is analyzed.

2. Fit method: the optimization is obtained through a study of the minimum relative error of a fit to the E_{ECL} variable, done with different configuration of cuts. This method will be widely explained in the section 4.4.2.

	SigProb	$\cos\theta_{\text{thrust.}}$	*R2*	$E_{\text{miss}} + p_{\text{miss}}$ (GeV)	p_{cand} (GeV)
e	0.018	1	0.64	4.74	0.4
μ	0.018	1	0.63	4.74	0.4
π	0.038	1	0.39	4.54	1.08
ρ	0.051	1	0.39	4.81	1.51
	Significance				
e	0.786				
μ	0.676				
π	0.725				
ρ	0.680				

Table 4.3: Best achieved Significance

A generic definition of the significance Z is the number of standard deviations which, in a normal distribution, would give the same p-value. According to Wilk's theorem, $-\log\lambda$, where λ is a likelihood-ratio that meets particular conditions, is distributed as a χ^2, then in general one holds $Z = \sqrt{-\log\lambda}$. The particular expression used is obtained from the general one in the limit case of event counting and $b \gg s$, and $Z \to s/\sqrt{b}$. In this expression, s stands for the signal events yield and b for background events one.
Pre-optimization cuts applied to the sample are:

1. Particle identification explained in the previous section;
2. $M_{bc} > 5.27\,\text{GeV}$;
3. $E_{\text{ECL}} < 1\,\text{GeV}$.

To select the best configuration of cuts with the significance method, a 5-dimensional matrix of $Z = s/\sqrt{b}$ has been created, since five selection variables have been used, determining Z from all the possible combinations of selection requirement:

1. *SigProb* > *test-value*;
2. $\cos\theta_{\text{thrust.}}$ < *test-value*;
3. *R2* < *test-value*;
4. $E_{\text{miss}} + p_{\text{miss}}$ < *test-value*;
5. p_{cand} > *test-value*;

The results are reported in tables 4.3.
For example, Figure 4.11 shows the Z values varying the selection requirements on $E_{\text{miss}} + p_{\text{miss}}$ (x-axis) and on p_{cand} (y-axis), while the other variables

are fixed to their best values. From these plots, it is evident that the candidate momentum p_{cand} is mostly effective for two-body decays of τ lepton (hadronic modes), while the missing energy is mostly effective for the three body decays (leptonic modes).

4.4 $B \to \tau\nu$ BRANCHING RATIO MEASUREMENT

The Branching Ratio of a decay, in particular $B \to \tau\nu$, can be estimated with the following formula:

$$BR(B \to \tau\nu) = \frac{N^{\text{true}}(B \to \tau\nu)}{N^{\text{true}}(B \to X)} = \frac{N^{\text{true}}(B \to \tau\nu)}{2L_{\text{int}}\sigma_{B^+B^-}} \tag{4.2}$$

where $N^{\text{true}}(B \to \tau\nu)$ is the number of B mesons that decay in $\tau\nu$ and $N^{\text{true}}(B \to X)$ is the total number of decays. The denominator of this fraction is the number of B pairs, and it is equal to $L_{\text{int}}\sigma_{B^+B^-} = 62.8\,\text{fb}^{-1} \times 0.5645\,\text{nb} \approx 35.5 \times 10^6$ ($62.8\,\text{fb}^{-1}$ is the luminosity of collision data analyzed). This number must be multiplied by 2 because this analysis is not charge-dependent, so both B can decay in $\tau\nu$.
The evaluation of $N^{\text{true}}(B \to \tau\nu)$ is performed by two measured quantities:

1. The number of fitted events: $N^{\text{reco}}(B \to \tau\nu)$;
2. The efficiency of the reconstruction (calculated using a MC simulation), as the ratio between the estimated amount of signal events that pass the selection (section 4.4.2) over the total number of events;

The definition of the efficiency for each reconstruction mode k, ε_k. is:

$$\varepsilon_k = \frac{N^{\text{reco}}(B \to \tau\nu \to k - \text{mode})}{N^{\text{generated}}(B \to \tau\nu)} \tag{4.3}$$

Therefore, the Branching Ratio value is obtainable through the following relation:

$$BR(B \to \tau\nu) = \frac{N^{\text{reco}}(B \to \tau\nu \to k - \text{mode})}{2L_{\text{int}}\sigma_{B^+B^-}\varepsilon_k} \tag{4.4}$$

4.4.1 Fit Process

For each τ decay mode k, the signal yield can be fitted with an extended likelihood, that uses the probability density function of the most discriminanting variable E_{ECL}.

$$\mathcal{L}_k = \frac{e^{-(n_{s,k}+n_{b,k})}}{N_k!} \prod_{i=1}^{N_k} \left\{ n_{s,k}\mathcal{P}_k^s(E_{i,k}) + n_{b,k}\mathcal{P}_k^b(E_{i,k}) \right\} \tag{4.5}$$

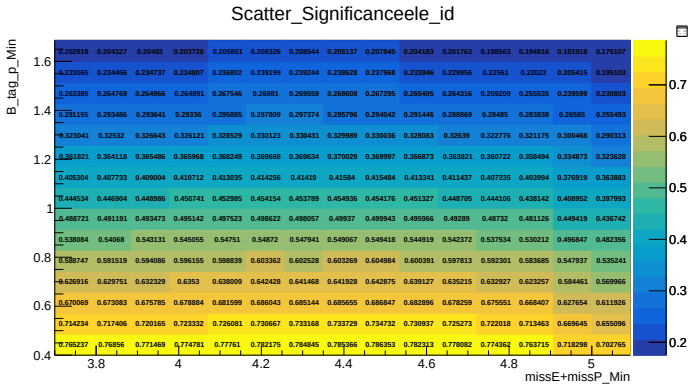

(a) Significance for electrons

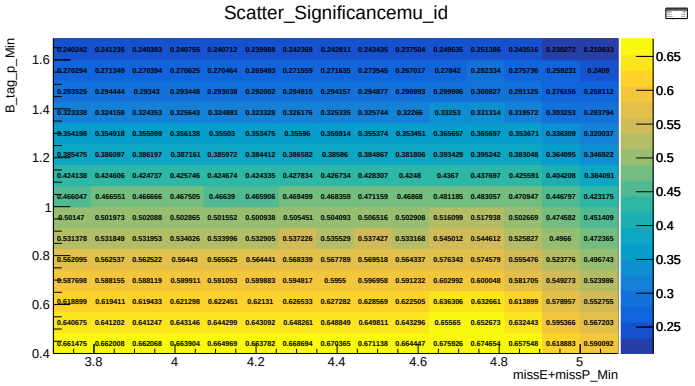

(b) Significance for muons

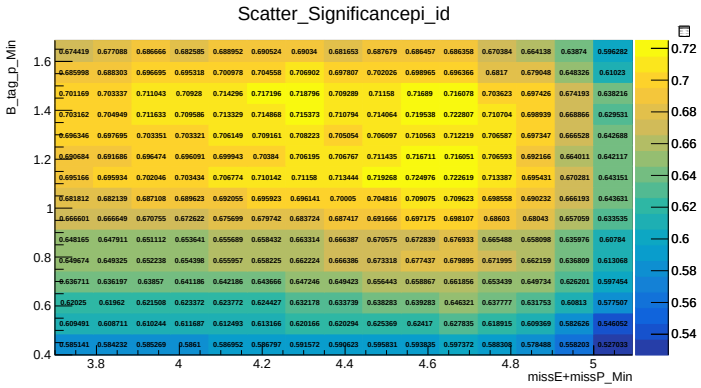

(c) Significance for pions

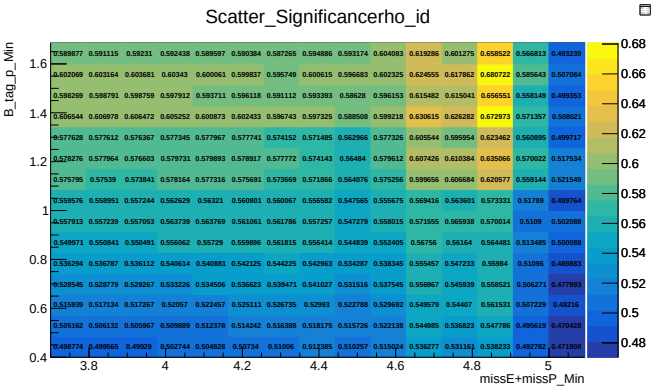

(d) Significance for ρs

Figure 4.11: Scatter plots for the *Significance* method

where $n_{s,k}$ is the signal yield, $n_{b,k}$ is the background yield, $E_{i,k}$ is the E_{ECL} value of the i^{th} event, $\mathcal{P}_k^{s,b}$ are the PDF of the signal (s) and the background (b).
The background and signal yields in each decay mode are permitted to float independently for each other in the fit, and the Branching Ratio is related to the signal yield:

$$n_{s,k} = 2L_{int}\sigma_{B^+B^-}\varepsilon_k BR(B \to \tau\nu) \tag{4.6}$$

The likelihood in Eq. 4.5 can be used to fit independently four signal yields, determining four independent measurements of the Branching Ratio $BR(B \to \tau\nu)$, using the Equation 4.6. Combining 4.5 and 4.6 and using $BR(B \to \tau\nu)$ as a common fitted parameter, a single value of Branching Ratio can be estimated (simultaneous fit).

4.4.2 Measurement Optimization

In addition to the counting method, described in 4.3.1, a more accurate method has been developed, performing the fit described above on TOY Monte Carlo pseudoexperiments. Previously described fit procedure have been performed on pseudo-datasets generated applying poissonian fluctuations on distributions taken from the Monte Carlo simulation. The fit results, i.e. the number of fitted signal events and its error, are recorded for all the pseudo-experiments, and the average values are taken to determine the configuration of cuts with the smallest relative error on the signal yield.
The used variables are:

1. *SigProb*;
2. $\cos\theta_{\text{thrust.}}$;
3. $R2$;
4. $E_{\text{miss}} + p_{\text{miss}}$;
5. p_{cand};

As before, a 5-dimensional matrix of relative errors σ_s/s has been filled.
An equivalent luminosity of $1\,\text{ab}^{-1}$ has been considered in order to have sufficient statistics to get stable results from the pseudoexperiments fits: a $63\,\text{fb}^{-1}$ luminosity sample would give 0 yield for the most of fits.
The results are reported in table 4.4.
The same analysis of the *Significance* method has been done, in Figure 4.12 scatter plots with the axis relative to p_{cand} and $E_{\text{miss}} + p_{\text{miss}}$ selection requirements are reported, while the other variables are fixed to their best ranges
With a more accurate method, based on TOY Monte Carlo, the results are almost compatible with the counting method.
The optimal selection requirement on $E_{\text{miss}} + p_{\text{miss}}$ is resulted to be very loose.

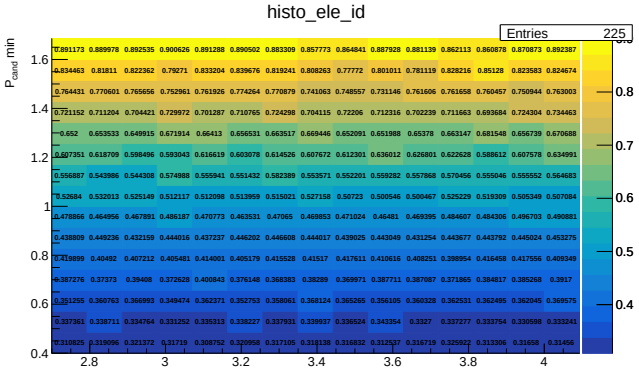

(a) Relative errors for electrons

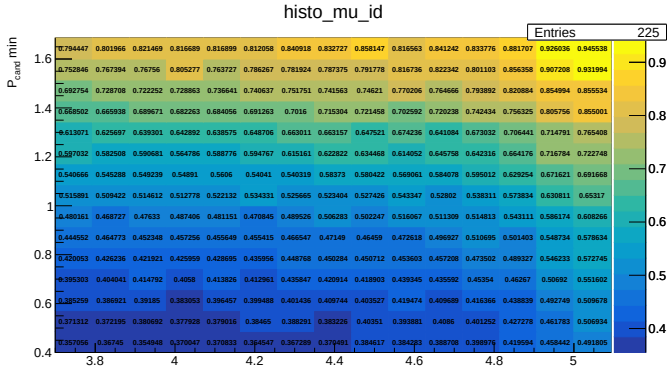

(b) Relative errors for muons

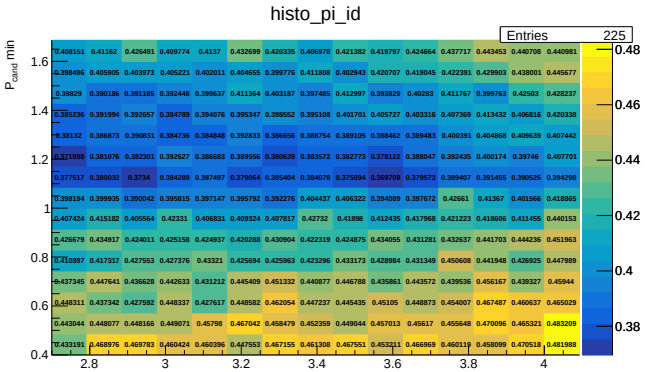

(c) Relative errors for pions

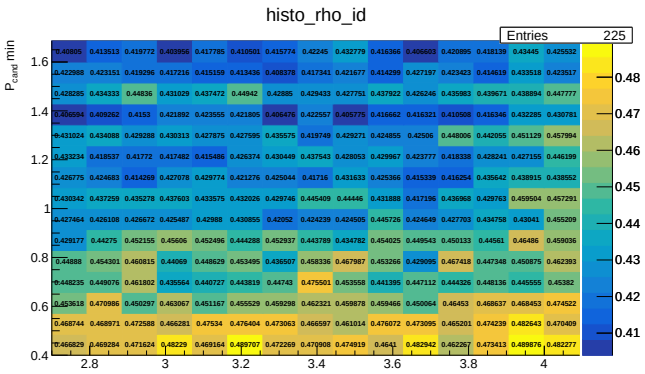

(d) Relative errors for ρs

Figure 4.12: Scatter plots for the *Fit* method

	SigProb	$\cos\theta_{\text{thrust.}}$	*R*2	$E_{\text{miss}} + p_{\text{miss}}$ (GeV)	p_{cand} (GeV)
e	0.015	1	0.63	3.07	0.4
μ	0.017	1	0.57	3.44	0.4
π	0.033	1	0.4	3.54	1.09
ρ	0.052	1	0.4	2.97	1.6
	Best Relative Error	s	σ_s		
e	0.304	107	32		
μ	0.354	87	31		
π	0.373	62	23		
ρ	0.411	38	15		

Table 4.4: Optimal Cuts and Best Relative Error

A fact that could not be predicted by looking at the $E_{\text{miss}} + p_{\text{miss}}$ distribution alone. Instead, as Figure 4.13 shows, E_{ECL} is correlated with it and selection on $E_{\text{miss}} + p_{\text{miss}}$ only affects the background shape at high values E_{ECL}, where the signal is almost negligible.

Optimization Algorithm in $\tau \to \rho\nu$ decay

The most abundant τ decay is the $\tau \to \rho\nu$ with a Branching Ratio equal to 25%. Moreover, this kind of decay is also the most difficult to study because of the presence of π^0 in the final state.
For the reasons mentioned above, for this channel additional variable are exploited, because the event is characterized by one charged track (π) and two photons. Since in the calorimeter may be many photon candidates, all the pairs are combined and the one with the smallest $\left|(p_\pi + p_\gamma^{(1)} + p_\gamma^{(2)})^\mu (p_\pi + p_\gamma^{(1)} + p_\gamma^{(2)})_\mu - m_\rho^2\right|$ is chosen. The following observables have been investigated:

- The photons spectrum;
- The momentum of the first son of ρ: p_{track};
- The π^0 energy: sum of two photons energies;
- The momentum of the ρ;
- The invariant masses of the ρ and π^0 mesons;
- $\Delta p/p = 2(p_\pi - p_{\pi^0})/(p_\pi + p_{\pi^0})$, this variable shows the ρ decay kinematics characteristics, related to the *pi*s momenta.

A further optimization has been performed, setting the selection requirements on variables listed in the section 4.4.2 and one of two following variables:

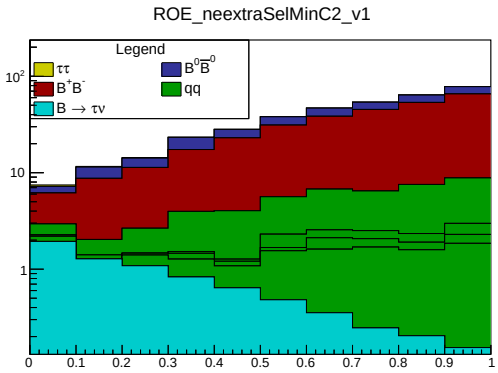

(a) E_{ECL} without "*missing* cut" (electron channel)

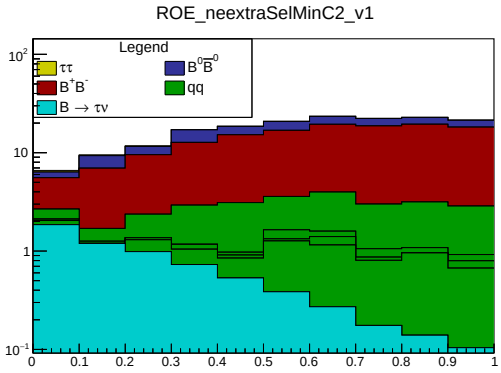

(b) E_{ECL} with "*missing* cut"

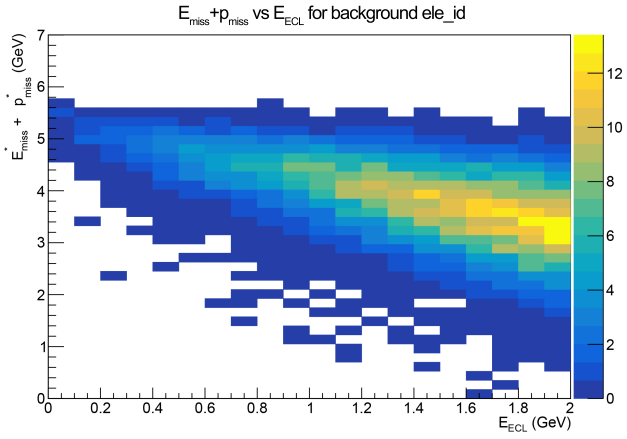

(c) Scatter Plot for Background

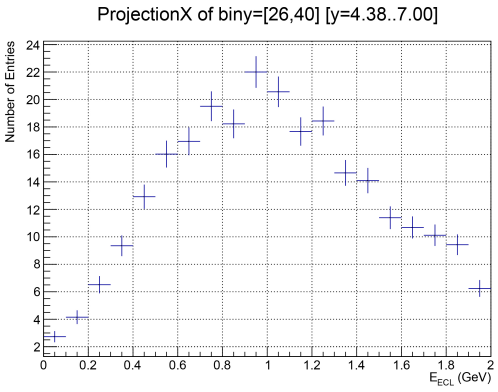

(d) Distribution of E_{ECL} with high missing energy

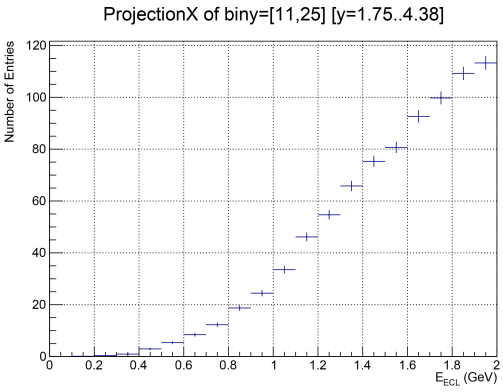

(e) Distribution of E_{ECL} with low missing energy

Figure 4.13: The background shape of the extra energy is shifted in the two different configurations (in the left one the plots shows the extra energy in a $E_{\mathrm{miss}} + p_{\mathrm{miss}}$ range equal to $[4.38, 7.00]$GeV, while in the right the interval is $[1.75, 4.38]$GeV)

- Energy of π^0 (sum of the photon couple energy);
- $\chi^2_{mm} = \frac{(m_\rho - m_\rho^{(\text{true})})^2}{\sigma^2_{m_\rho}} + \frac{(m_{\pi^0} - m_{\pi^0}^{(\text{true})})^2}{\sigma^2_{m_{\pi^0}}}$.

In Figure 4.15, the 2D matrices have been reported, in which the axis are represented by the selection requirements on p_{cand} and the ρ variable, both χ^2_{mm} and E_{π^0}. It is possible to note that only the π^0 energy is useful for the background rejection, while, for the other variables, the signal and backgrounds have similar distributions.
The table 4.5 shows all the selection requirements found for the ρ channel.

	SigProb	$\cos\theta_{\text{thrust.}}$	*R2*	$E_{\text{miss}} + p_{\text{miss}}$ (GeV)	p_{cand} (GeV)
ρ	0.052	1	0.4	2.97	1.6
	E_{π^0} (MeV)	Best Relative Error	s	σ_s	
ρ	140	0.411	38	15	

Table 4.5: Optimal Cuts and Best Relative Error for ρ channel

4.4.3 Efficiency Measurement

The efficiency to reconstruct a signal decay in k-mode is given by:

$$\varepsilon_k = \frac{N^{\text{reco}}(B \to \tau\nu \to k - \text{mode})}{N^{\text{generated}}(B \to \tau\nu)} \tag{4.7}$$

The efficiency ε_k is needed to relate the signal yield in the mode k (a fit parameter in the likelihood function in eq. 4.5) to the $BR(B \to \tau\nu)$ using equation 4.6. The Monte Carlo simulation of the signal events is used to determine the efficiencies ε_k and the Probability density functions f the E_{ECL} distribution used in the fit. The Monte Carlo simulations has been used also to estimate the true composition of the events that have been reconstructed in the mode k. Table 4.6 shows the breakdown of each reconstructed mode in terms of its sources. The last line show the total reconstruction efficiency ε_k for each reconstructed mode. It is evident from the results that most of the events that are reconstructed in the electron and muon modes come from real τ decays to electrons and muons, respectively. Instead, events reconstructed as $\tau \to \pi\nu$ mainly come from real $\tau \to \pi\nu$ events and from $\tau \to \rho\nu$ events, where the π^0 from ρ decay is not reconstructed. Conversely, the events assigned to the ρ mode can come from real $\tau \to \rho\nu$, but also from $\tau \to \pi\pi^0\pi^0$ decays where the

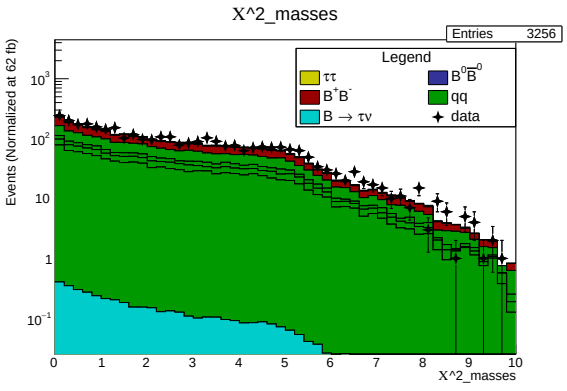

(a) $\chi^2_m = \frac{(m_\rho - m_\rho^{(\text{real})})^2}{\sigma^2_{m_\rho}} + \frac{(m_{\pi^0} - m_{\pi^0}^{(\text{real})})^2}{\sigma^2_{m_{\pi^0}}}$

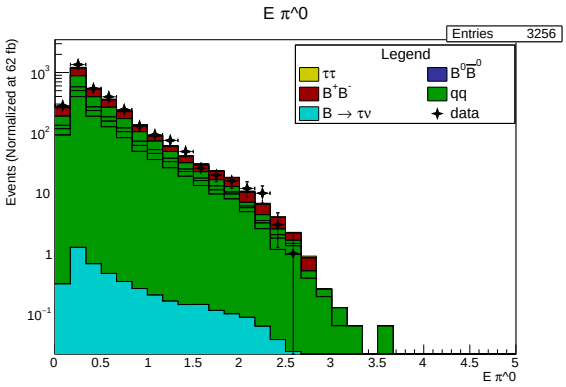

(b) π^0 energy

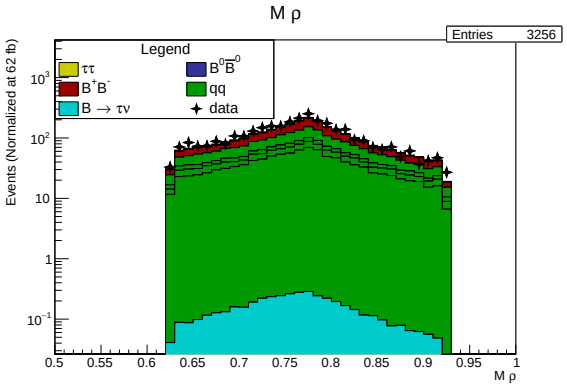

(c) $\pi\gamma\gamma \to \rho$ invariant mass

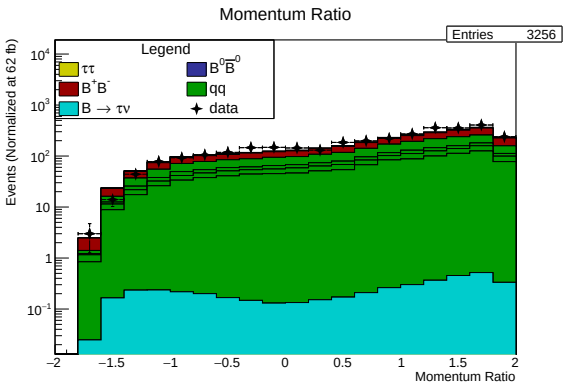

(d) $2(p_\pi - p_{\pi^0})/(p_\pi + p_{\pi^0})$

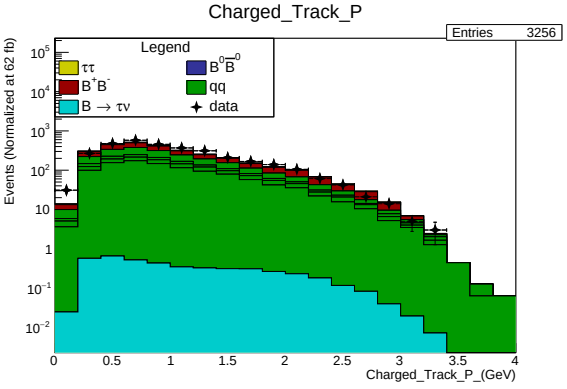

(e) π momentum

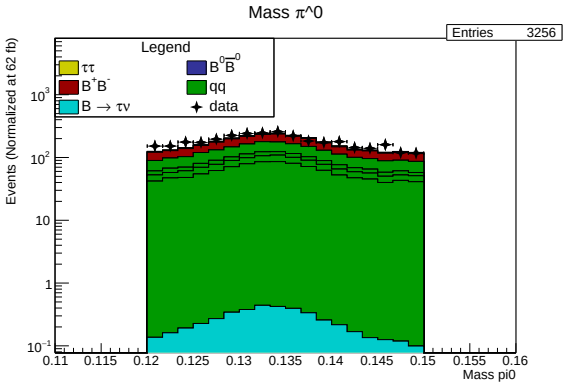

(f) m_{π^0}

Figure 4.14: Generic variables study about $\tau \to \rho\nu$

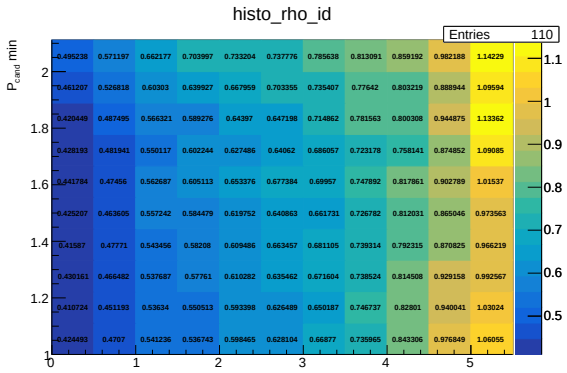

(a) Relative Error Scatter Plot between p_ρ and χ^2_{mm}

(b) Relative Error Scatter Plot between p_ρ and E_{π^0}

Figure 4.15: 2D matrix for the ρ decay optimization

	e-id	μ-id	π-id	ρ-id
real $e\nu\nu$	97.08%	0.057%	0.22%	0.03%
real $\mu\nu\nu$	0.38%	89.08%	1.68%	0.12%
real $\pi\nu$	0.97%	3.53%	57.97%	11.56%
real $\pi\pi^0\nu$	0.92%	4.50%	25.36%	58.29%
other	0.63%	2.81%	14.76%	30.00%
total (ε_k)	8.8×10^{-4}	7.32×10^{-4}	5.1×10^{-4}	3.0×10^{-4}

Table 4.6: Cross-Feed values

second π^0 is not considered and from $\tau \to \pi\nu$ with a π^0 from combinatorial background added.
As an additional example, Figure 4.16 shows the contamination in the ρ channel from the events that are not true ρ in the observable $\Delta p/\overline{p}$, where $\Delta p = p_\pi - p_{\pi^0}$ and $\overline{p} = 1/2(p_\pi + p_{\pi^0})$.

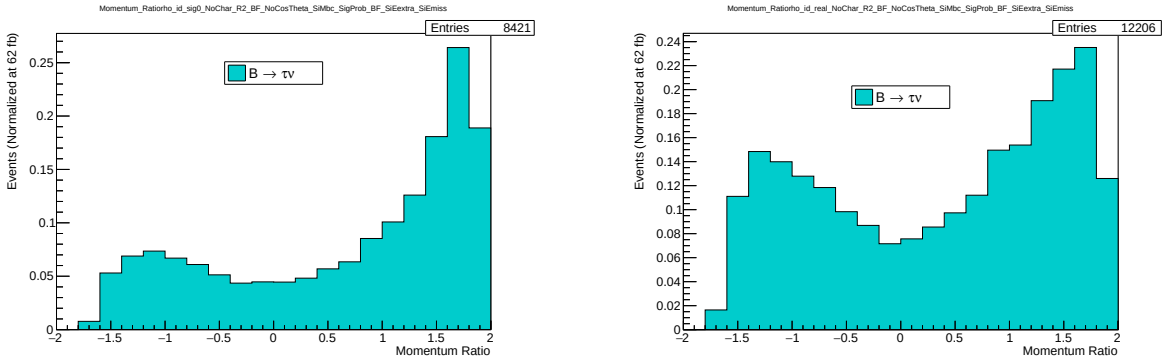

(a) Fake ρs

(b) True ρs

Figure 4.16: Contamination in the ρ channel due to similar decays, like $\tau \to \pi\pi^0\pi^0$

4.5 BELLE II SENSITIVITY ON $B \to \tau\nu$ BRANCHING RATIO

In this section, the Branching ratio measurement is presented. Because of the Belle II policy it is not yet possible to see and show the real experimental dataset in order to keep the analysis blind, until a formal permission is given under the internal review of this work. Therefore, the sensitivity of $B \to \tau\nu$ Branching Ratio measurement as a function of accumulated statistics is given. For this purpose, a simulation of several number of pseudoexperiments with different luminosity has been used. The measurement is performed in two ways:

FIT TO THE SIGNAL YIELD : the fit is repeated for each channel independently with a hypothetic luminosity equal to $1\,\text{ab}^{-1}$, assuming a Branching Ratio of 1.09×10^{-4}. This results in four independent determinations of the Branching Ratio. An additional fit is performed considering the 4 channels summed together at increasing luminosities from $100\,\text{fb}^{-1}$ to $1000\,\text{fb}^{-1}$ in order to study how the relative error decreases with increasing statistic.

SIMULTANEOUS FIT : a simultaneous fit has been performed combining the four likelihoods of Eq.4.5 in a single likelihood with Branching Ratio

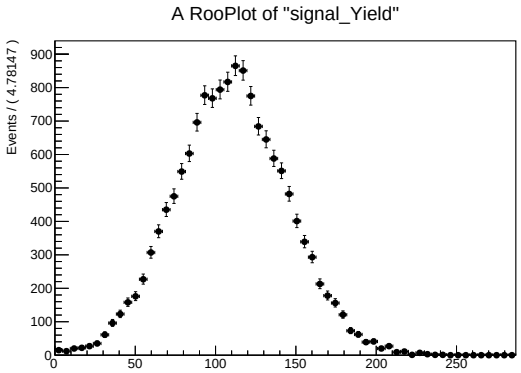

(a) Signal Yield results of the Toy-MC study for the e channel

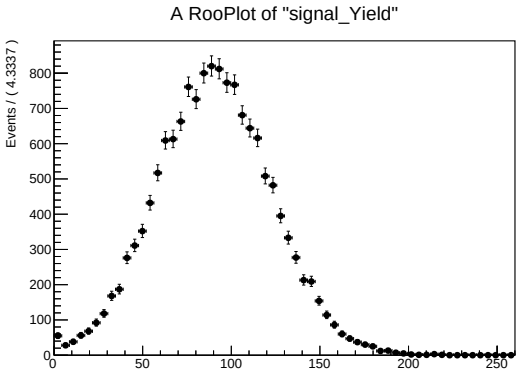

(b) Signal Yield results of the Toy-MC study for the μ channel

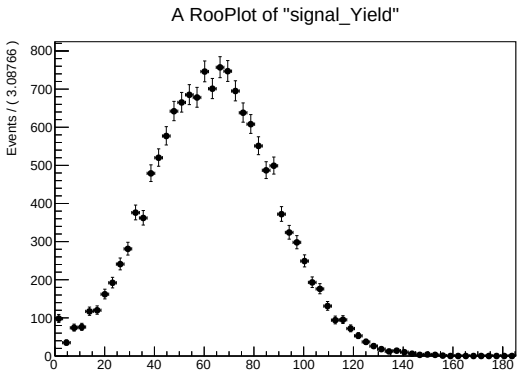

(c) Signal Yield results of the Toy-MC study for the π channel

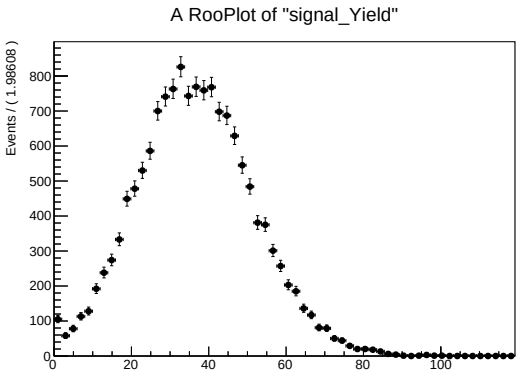

(d) Signal Yield results of the Toy-MC study for the ρ channel

Figure 4.17: Signal Yield results of the Toy-MC study for an equivalent luminosity equal to $1\,\text{ab}^{-1}$

$B \to \tau\nu$ as a common parameter to be fitted. This kind of study has been implemented with an increasing luminosity as in the single fit (4.5).

Single Fits

Figure 4.17 show the fitted the signal yields obtained with TOY Monte Carlo for the 4 channels (a $n_{s,k}$ distribution for each decay channel). The expected signal yield is the average of the fitted values.
Table 4.7 shows the fitted signal yield and related Branching Ratio for a simulated statistic of $1\,\text{ab}^{-1}$.

As table 4.7 reports, with $1\,\text{ab}^{-1}$ dataset the expected fitted branching fractions present no bias, i.e. the fitted Branching Ratio are in agreement with the input value o $BR = 1.09 \times 10^{-4}$ that has been used to generate the pseudodatasets. The first approach considered is to sum all the E_{ECL} probability density function and make a TOY-MC study for the 4 decay channels together.

Decay Channel	ε_k	Signal Yield	$BR(B \to \tau\nu)$
$\tau \to e\nu\nu$	8.8×10^{-4}	109 ± 35	$(1.09 \pm 0.39) \times 10^{-4}$
$\tau \to \mu\nu\nu$	7.3×10^{-4}	90 ± 32	$(1.10 \pm 0.39) \times 10^{-4}$
$\tau \to \pi\nu$	5.1×10^{-4}	64 ± 25	$(1.10 \pm 0.42) \times 10^{-4}$
$\tau \to \rho\nu$	3.0×10^{-4}	36 ± 15	$(1.10 \pm 0.45) \times 10^{-4}$

Table 4.7: Summary of efficiencies ε_k and fit results for each τ decay channel considered

In this case the same analysis has been repeated for many integrated luminosity values (from 100 to 1000 fb^{-1}). The fitted value with a 1 ab^{-1} luminosity is:

$$BR_{\text{sum}} = (1.09 \pm 0.21) \times 10^{-4} \tag{4.8}$$

The Figure 4.18 reports four examples of Signal Yield values with different luminosity values and the Figure 4.20a reports the relative error decreasing in relation to the luminosity.

Simultaneous Fit

This kind of alghorithm foresees a minimization of a likelihood, equal to the sum of all the $\mathcal{L}_k$ related to each decay mode. This method takes into account the cross-feeds in each subset and the different particle efficiencies.
For this reason, the fitted value is not the Signal Yield, but the Branching Ratio, that is the common variable in all the likelihoods. The fitted value with a 1 ab^{-1} luminosity is:

$$BR_{\text{sim}} = (1.09 \pm 0.20) \times 10^{-4} \tag{4.9}$$

The Figure 4.19 reports the fit results for 5000 pseudoexperiments at four different luminosities.Figure 4.20b shows the relative error as a function of the luminosity.
In Figure 4.20c, the trend of relative uncertainties for both methods has been shown.

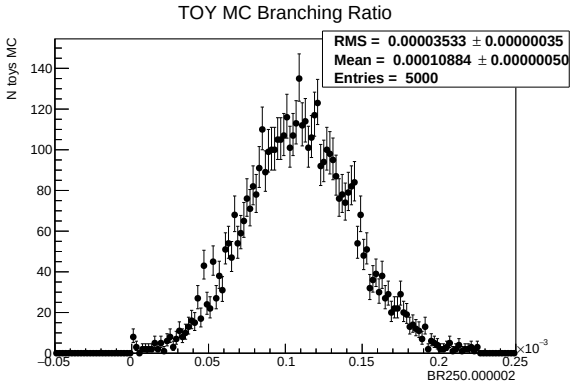

(a) Signal Yield results of the Toy-MC study for $L = 250\,\text{fb}^{-1}$

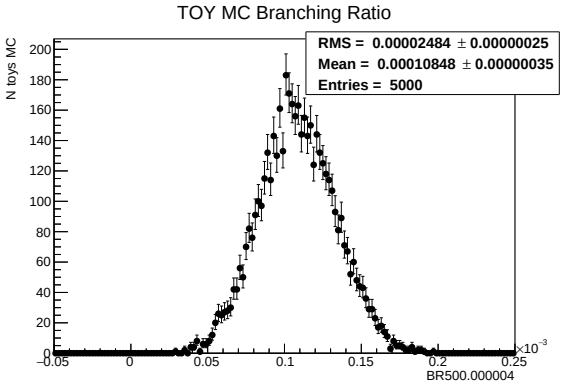

(b) Signal Yield results of the Toy-MC study for $L = 500\,\text{fb}^{-1}$

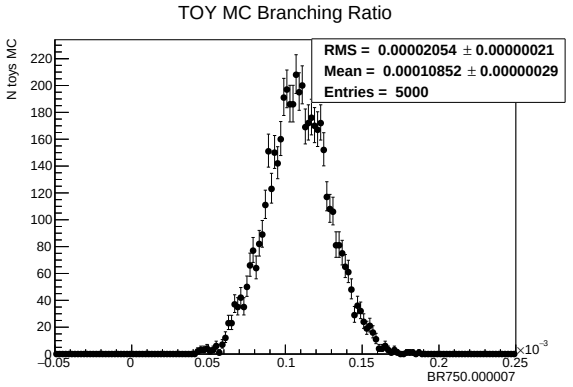

(c) Signal Yield results of the Toy-MC study for $L = 750\,\text{fb}^{-1}$

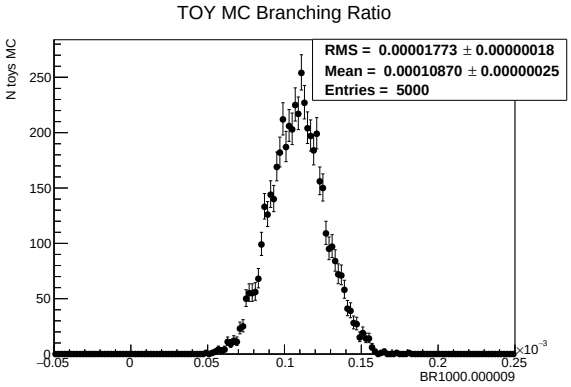

(d) Signal Yield results of the Toy-MC study for $L = 1000\,\text{fb}^{-1}$

Figure 4.18: Signal Yield results of the Toy-MC study at different luminosity values for all the channels

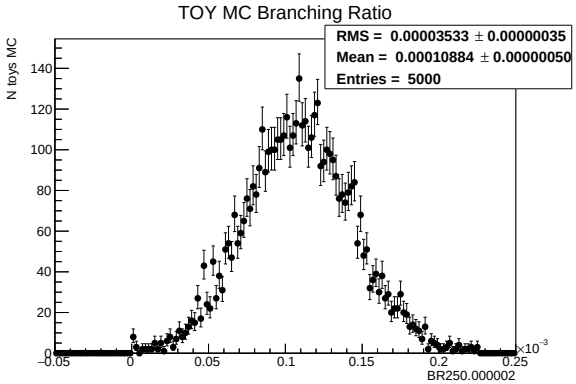

(a) Signal Yield results of the Toy-MC study for $L = 250\,\text{fb}^{-1}$

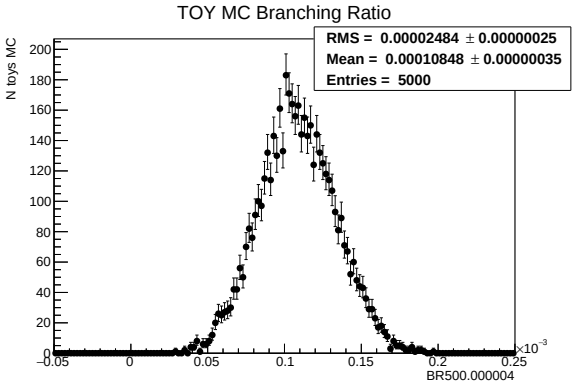

(b) Signal Yield results of the Toy-MC study for $L = 500\,\text{fb}^{-1}$

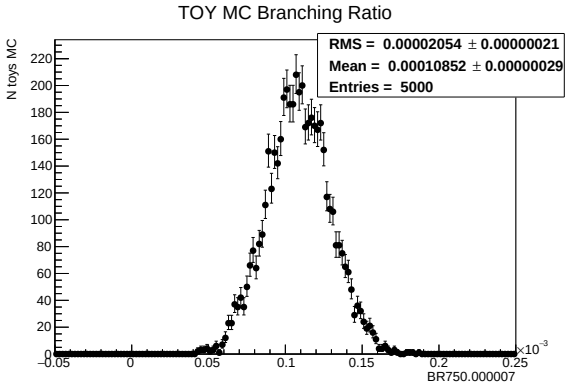

(c) Signal Yield results of the Toy-MC study for $L = 750\,\text{fb}^{-1}$

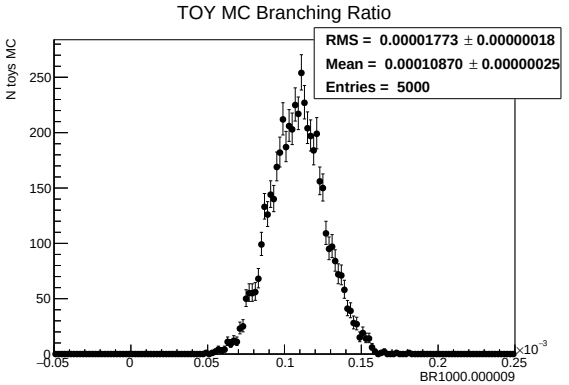

(d) Signal Yield results of the Toy-MC study for $L = 1000\,\text{fb}^{-1}$

Figure 4.19: BR results of the simultaneous Toy-MC study at different luminosity values

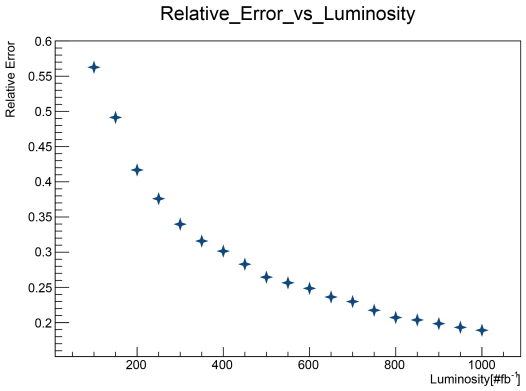

(a) Relative Errors in relation to luminosity values for the sum of all decay channels

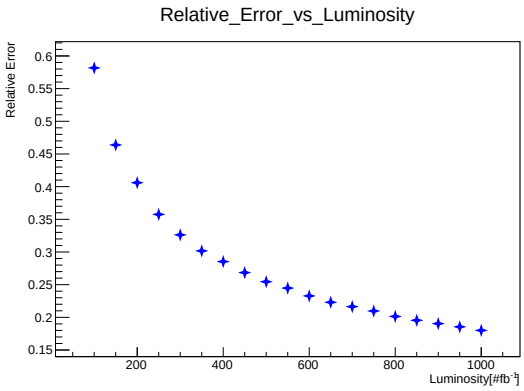

(b) Relative Errors in relation to luminosity values for the simultaneous fit

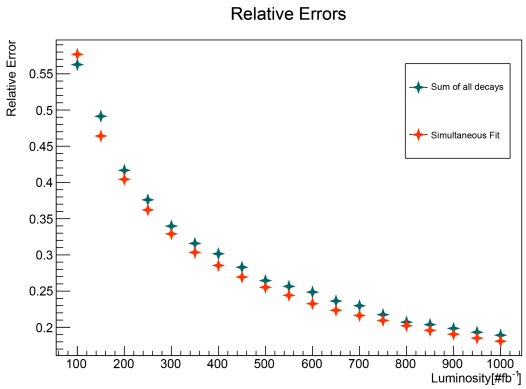

(c) Relative Errors in relation to luminosity values: two methods compared

Figure 4.20: Relative Errors in relation to luminosity values

CONCLUSIONS

In this thesis project, the analysis of the $B \to \tau\nu$ Branching Ratio has been performed and the sensitivity of the Belle II experiment has been studied. Previous measurements, done by BABAR and Belle, used an integrated luminosity of $400\,\text{fb}^{-1}$ and $700\,\text{fb}^{-1}$, respectively. Belle II goal is much ambitious, as the next couple of years the experiment is expected to accumulate an integrated luminosity of $1\,\text{ab}^{-1}$, that will reach $50\,\text{ab}^{-1}$ by the end of the data taking.
This study performed in the thesis indicates that a 20% uncertainty in the measurement of the branching fraction $BR(B \to \tau\nu)$ is achievable with $1\,\text{ab}^{-1}$, in detail:

$$BR(B \to \tau\nu)_{\text{sim}} = (1.09 \pm 0.20) \times 10^{-4} \tag{4.10}$$

$$BR(B \to \tau\nu)_{\text{sum}} = (1.09 \pm 0.21) \times 10^{-4} \tag{4.11}$$

The first obtained with a simultaneous fit of the four tau decay channels and the second considering the sum of the four categories.
Both the results are in good agreement with each other and with the value of Branching Ratio used as input (pseudo-datasets are generated with an input Branching Ratio of $(1.09 \pm 0.24) \times 10^{-4}$).
Moreover, the significance of the $B \to \tau\nu$ signal as a function of integrated luminosity L_{int} has been studied, so that a 5σ measurement will be achieved at roughly $850\,\text{fb}^{-1}$ (Figure A).

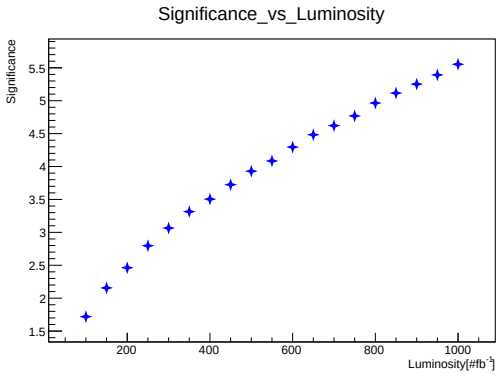

Figure A: Significance vs Luminosity

Future developments may concern the optimization of the signal selection to reduce the statistical uncertainty on the signal yield, refining the continuum rejection and estimating the peaking background contribution in order to reject it.

BIBLIOGRAPHY

[1] S. Abachi et al. "Observation of the Top Quark." In: *Physical Review Letters* 74.14 (Apr. 1995), pp. 2632–2637. ISSN: 1079-7114. DOI: 10.1103/physrevlett.74.2632. URL: http://dx.doi.org/10.1103/PhysRevLett.74.2632.

[2] I. Adachi et al. "Evidence for $B^- \to \tau^- \bar{\nu}_\tau$ with a Hadronic Tagging Method Using the Full Data Sample of Belle." In: *Phys. Rev. Lett.* 110.13 (2013), p. 131801. DOI: 10.1103/PhysRevLett.110.131801. arXiv: 1208.4678 [hep-ex].

[3] K. Adamczyk et al. "The Belle II silicon vertex detector assembly and mechanics." In: *Nucl. Instrum. Meth. A* 845 (2017). Ed. by G. Badurek et al., pp. 38–42. DOI: 10.1016/j.nima.2016.03.100.

[4] Nils Braun et al. "The Belle II Core Software." In: *Computing and Software for Big Science* 3 (Nov. 2018). DOI: 10.1007/s41781-018-0017-9.

[5] Thomas E. Browder et al. "New physics at a Super Flavor Factory." In: *Rev. Mod. Phys.* 81 (4 Dec. 2009), pp. 1887–1941. DOI: 10.1103/RevModPhys.81.1887. URL: https://link.aps.org/doi/10.1103/RevModPhys.81.1887.

[6] Nicola Cabibbo. "Unitary Symmetry and Leptonic Decays." In: *Phys. Rev. Lett.* 10 (12 June 1963), pp. 531–533. DOI: 10.1103/PhysRevLett.10.531. URL: https://link.aps.org/doi/10.1103/PhysRevLett.10.531.

[7] SuperB Collaboration. *SuperB: A High-Luminosity Asymmetric e+ e- Super Flavor Factory. Conceptual Design Report*. 2007. arXiv: 0709.0451 [hep-ex].

[8] S. L. Glashow, J. Iliopoulos, and L. Maiani. "Weak Interactions with Lepton-Hadron Symmetry." In: *Phys. Rev. D* 2 (7 Oct. 1970), pp. 1285–1292. DOI: 10.1103/PhysRevD.2.1285. URL: https://link.aps.org/doi/10.1103/PhysRevD.2.1285.

[9] LeptonID group and Belle II Collaboration. "Muon and electron identification efficiencies and hadron-lepton mis-identification rates at Belle II for Moriond 2021." In: (Mar. 2021). For Moriond 2021.

[10] S. W. Herb et al. "Observation of a Dimuon Resonance at 9.5 GeV in 400-GeV Proton-Nucleus Collisions." In: *Phys. Rev. Lett.* 39 (5 Aug. 1977), pp. 252–255. DOI: 10.1103/PhysRevLett.39.252. URL: https://link.aps.org/doi/10.1103/PhysRevLett.39.252.

[11] Wei-Shu Hou. "Enhanced charged Higgs boson effects in $B^- \to \tau\overline{\nu}, \mu\overline{\nu}$ and $b \to \tau\overline{\nu} + X$." In: *Phys. Rev. D* 48 (5 Sept. 1993), pp. 2342–2344. DOI: 10.1103/PhysRevD.48.2342. URL: https://link.aps.org/doi/10.1103/PhysRevD.48.2342.

[12] Thomas Keck. *Machine Learning at the Belle II Experiment: The Full Event Interpretation and Its Validation on Belle Data*. 1st ed. Springer Theses. Springer International Publishing, 2018, pp. 63–100. ISBN: 978-3-319-98248-9,978-3-319-98249-6. URL: https://www.springer.com/gp/book/9783319982489.

[13] E Kou et al. "The Belle II Physics Book." In: *Progress of Theoretical and Experimental Physics* 2019.12 (Dec. 2019). ISSN: 2050-3911. DOI: 10.1093/ptep/ptz106. URL: http://dx.doi.org/10.1093/ptep/ptz106.

[14] J. P. Lees et al. "Evidence of $B^+ \to \tau^+\nu$ decays with hadronic B tags." In: *Phys. Rev. D* 88 (3 Aug. 2013), p. 031102. DOI: 10.1103/PhysRevD.88.031102. URL: https://link.aps.org/doi/10.1103/PhysRevD.88.031102.

[15] Luca Lista. *Statistical Methods for Data Analysis in Particle Physics*. Vol. 909. Springer, 2016. ISBN: 978-3-319-20175-7, 978-3-319-20176-4. DOI: 10.1007/978-3-319-20176-4.

[16] J. Neyman and Harold Jeffreys. "Outline of a Theory of Statistical Estimation Based on the Classical Theory of Probability." In: *Philosophical Transactions of the Royal Society of London. Series A, Mathematical and Physical Sciences* 236.767 (1937), pp. 333–380. DOI: 10.1098/rsta.1937.0005. eprint: https://royalsocietypublishing.org/doi/pdf/10.1098/rsta.1937.0005. URL: https://royalsocietypublishing.org/doi/abs/10.1098/rsta.1937.0005.

[17] Lincoln Wolfenstein. "Parametrization of the Kobayashi-Maskawa Matrix." In: *Phys. Rev. Lett.* 51 (1983), p. 1945. DOI: 10.1103/PhysRevLett.51.1945.

[18] P.A. Zyla et al. "Review of Particle Physics." In: *PTEP* 2020.8 (2020), p. 083C01. DOI: 10.1093/ptep/ptaa104.